On the role of phyllosilicates on fault lubrication: Insight from micro- and nanostructural investigations on talc friction experiments

Sébastien Boutareaud,[1] Takehiro Hirose,[2] Muriel Andréani,[3] Matej Pec,[4] Dan-Gabriel Calugaru,[5] Anne-Marie Boullier,[6,7] and Mai-Linh Doan[6]

Received 8 November 2011; revised 18 May 2012; accepted 13 June 2012; published 11 August 2012.

[1] Exposures of mature faults at the Earth's surface show that in the shallow crust some of co-seismic slip occurs within a narrow phyllosilicate-rich gouge material. Mechanical behavior of phyllosilicates sheared at seismic slip-velocities remains a complex issue as suggested by the experimental and theoretical studies reported so far. Talc represents a simple case for common phyllosilicates in natural faults and therefore we chose talc as an analogue to better understand the mechanical behavior of clay-rich mature crustal faults. We present a series of high-velocity friction experiments conducted on talc at 1.31 m s^{-1} and normal stresses of 0.3–1.8 MPa for wet and dry conditions. At 1 MPa normal stress, both wet and dry experiments show a slip-weakening behavior, however, with a higher decreasing rate in wet conditions. Dynamic shear stress evolves from a peak value of 0.24–0.52 MPa down to a residual state value of 0.08–0.18 MPa in wet conditions, and from a peak value of 0.46–1.17 MPa down to a residual state value of 0.12–0.62 MPa in dry conditions. Based on a detailed microstructural analysis down to the nanoscale, we propose thermal-pressurization as a possible slip-weakening mechanism for wet conditions. On the contrary, in dry conditions the long-lasting weakening is interpreted to be due to a combination of *i*) progressive disappearance of geometrical incompatibilities, *ii*) solid lubrication of talc lamellae, and *iii*) powder lubrication by nanometric aggregates. We conclude that initial gouge humid conditions and inherited fabric from past sliding may have large influence on the slip-weakening for subsequent slip.

Citation: Boutareaud, S., T. Hirose, M. Andréani, M. Pec, D.-G. Calugaru, A.-M. Boullier, and M.-L. Doan (2012), On the role of phyllosilicates on fault lubrication: Insight from micro- and nanostructural investigations on talc friction experiments, *J. Geophys. Res.*, *117*, B08408, doi:10.1029/2011JB009006.

1. Introduction

[2] During an earthquake, complex thermo-poro-mechanical and physico-chemical processes control fault friction [*Sibson*, 1989; *Wintsch et al.*, 1995; *Rice*, 2006; *Di Toro et al.*, 2011]. Seismology paved the way for earthquake mechanics studies by interpreting seismic waves from active faults [*Lee et al.*, 2002]. However, seismology remains an indirect technique of study by which it is impossible to fully address issues such as variations of dynamic shear stress during earthquake [*Bouchon*, 1997], energy budget of an earthquake, or the physical processes that occur during earthquake rupture propagation (*Kanamori and Brodsky* [2004]; *Lapusta* [2009]; see *Di Toro et al.* [2012] for a complete review). Laboratory rotary shear experiments have been conducted for more than 15 years to gain direct information on the physico-chemical mechanisms that occur during earthquake faulting. The mechanical behavior of simulated faults seems to be coherent with seismological studies of major studied earthquakes [e.g., *Mizoguchi et al.*, 2007a; *Sone and Shimamoto*, 2009; *De Paola et al.*, 2011], and experimental and natural gouge microstructures show similar characteristics [e.g., *Mizoguchi et al.*, 2009b; *Boutareaud et al.*, 2010].

[3] Recent low to high slip-velocity experiments [*Sone and Shimamoto*, 2009] allowed reproduction of the kinematic slip history of a major earthquake rupture (1999 Chi-Chi, Taiwan, Earthquake) [*Ji et al.*, 2003]. The frictional behavior of the simulated fault has shown that faults undergo a sequence of strengthening, weakening and healing during acceleration and deceleration of slip. These results suggest that fault ruptures propagate in a pulse-like mode [*Heaton*,

[1]Geologisches Institut, ETH Zürich, Zürich, Switzerland.
[2]Kochi Institute for Core Sample Research, JAMSTEC, Kochi, Japan.
[3]Laboratoire de Géologie de Lyon: Terre, Planètes, Environnement, UMR 5276, Ecole Normale Supérieure de Lyon et Université Lyon I, Lyon, France.
[4]Geological Institute, University of Basel, Basel, Switzerland.
[5]Institut NEEL, UPR 2940 CNRS, Grenoble, France.
[6]Institut des Sciences de la Terre, CNRS, University Joseph Fourier, Grenoble, France.
[7]International Laboratory (LIA) ADEPT, France-Taiwan, CNRS, NSC, Taipei, Taiwan.

Corresponding author: S. Boutareaud, Geologisches Institut, ETH Zürich, Sonneggstr. 5, Zürich CH-8092, Switzerland. (sebastien.boutareaud@erdw.ethz.ch)

0148-0227/12/2011JB009006

1990], in which the risetime of fault slip is much shorter than the total duration of the event. The strong initial strengthening associated with increasing slip-velocity has already been observed in metallurgy in the 0.01–0.1 m s^{-1} range [*Lim et al.*, 1989] and should impose a barrier for rupture growth into large earthquakes. This strengthening may prevent easy generation of large earthquakes and may have a major role in determining the final rupture dimension. Thus, the first meters of slip during acceleration appear to be critical to overpass the strength barrier and to develop an appropriate slip-weakening mechanism. The cause of the initial strengthening at the microscopic scale that influences the nucleation of earthquakes has received large interest from experimentalists for low displacement rates [*Paterson and Wong*, 2004; *Mair and Abe*, 2008; *Niemeijer et al.*, 2010]. However, little attention has been paid to seismic slip-velocities so far [e.g., *Mizoguchi et al.*, 2009a, 2009b; *Sone and Shimamoto*, 2009].

[4] This paper aims to investigate the weakening mechanisms activated during co-seismic slip along a phyllosilicate-rich fault gouge, since multiple mechanisms can potentially occur within the slip zone [e.g., *Gratier and Gueydan*, 2007; *Bizzarri*, 2009; *Niemeijer et al.*, 2010; *De Paola et al.*, 2011]. Further, we aim at investigating the effect of pre-existing gouge fabric from an initial slip on the amplitude of the subsequent co-seismic peak shear stress and so the occurrence of consecutive thermally activated slip-weakening mechanism(s). Talc has been chosen because it represents a chemically simple case (low water adsorption, high thermal decomposition temperature, no chemical processes, no oxidation) among the phyllosilicates that compose some mature faults [*Vrolijk and van der Pluijm*, 1999]. We report a series of rotary shear experiments conducted on a pure talc powder at 1.31 m s^{-1} over a range of normal stresses (0.3–1.8 MPa). We have characterized microstructure evolution with increasing displacement by scanning electron microscopy (SEM) and transmission electron microscopy (TEM) in order to investigate how they correlate with the mechanical behavior. Microstructure development correlates with the mechanical behavior. Weakening is accompanied by re-orientation of talc grain (001) cleavage planes parallel to the (C-) shear plane direction, and the development of nanometric aggregates. We then discuss possible implications of gouge fabric development during the seismic cycle for mature crustal faults.

2. Sample Assembly and Experimental Conditions

2.1. Characterization of Initial Material

[5] Talc ($Mg_3Si_4O_{10}(OH)_2$) is a trioctahedral phyllosilicate with a structure composed of stacking sequences of tetrahedral-octahedral-tetrahedral (*TOT*) layers in the monoclinic system. This sheeted structure is hydrophobic, completely compensated and stable. Weak Van der Waals force bonds the *TOT* sequences. They lead to a strong mechanical anisotropy responsible for an excellent plane of cleavage parallel to the stacking plane (001), and a high tendency for interlayer delamination and slip.

[6] The talc gouge used in our experiments is made from a natural talc schist powder acquired from VWR Corporation (http://www.vwrsp.com). X-ray Diffraction (XRD) and X-ray Fluorescence (XRF) analyses show that the talc powder is a high-purity monomineralic aggregate with about 0.01 wt.% of solid impurities (orthopyroxene), and 5.9 wt.% of constitutive water (i.e., from the crystal structure). It is composed of platy-angular to subangular grains with a long axis ranging from 1 to 100 μm (25 μm as a mean), with an axial ratio of about 0.33 for the 25 μm-thick particles, and 0.14 for the 5 μm-thick particles.

[7] Thermogravimetric-differential thermal analyses (TG-DTA) have been conducted on the talc schist powder in a helium environment for dynamic heating conditions of 10 and 50°C min^{-1}. This type of analysis provides data on the thermally activated mineralogical transformations that can possibly occur during high-velocity friction experiments. From 20 to 120°C, adsorbed water is released. Then up to 500°C interlayer water is driven off. From 500°C to 900°C, dehydroxylation of talc schist (i.e., breakage of the Mg-OH bonds) starts with a weight reduction of about 1%. Then, from 900°C to 1300°C, about 4.8 wt.% of water is released. The total amount of water loss from 500°C to 1300°C is similar to the loss on ignition calculated from XRF analyses. At around 1300°C, crystallization of enstatite with formation of amorphous silica is observed. These results are consistent with *Evans and Guggenheim* [1988] and *Piga et al.* [1992], but do not match reported data from *Ward* [1975] and *Wesolowski* [1984], for which crystallization of enstatite starts earlier (i.e., at about 720°C). Enstatite crystallization from talc dehydroxylation localized in the shearing zone at 860°C has also been reported by *Escartín et al.* [2008] during triaxial experiments suggesting a role of deformation on reaction kinetics. But in static experiments, we attribute this apparent discrepancy of reaction kinetics between authors to differences in the rate of temperature increase and in the size distribution of grains: the smaller the grain size, the larger the specific surface and the faster reactions take place.

2.2. Experimental Setup and Method

[8] The experimental fault consists of a 25 mm-diameter gabbro cylinder cut perpendicular to the revolution axis. Cylinder surfaces are ground with a 220# grid to obtain rough wall surfaces in order to promote shear throughout the gouge layer (Figure 1). Cylinders are assembled with an intervening layer of ca. 1–1.5 mm-thick talc gouge. We put 0.4 wt.% of distilled water into the gouge for wet tests. The assembly is then placed in the high-velocity rotary-shear apparatus [*Shimamoto and Tsutsumi*, 1994], where one cylinder remains stationary while the other rotates. See *Hirose and Shimamoto* [2005] and *Mizoguchi et al.* [2007a] for complete experimental setup and procedure. A Teflon sleeve surrounds the fault to avoid gouge material or liquid water expulsion during rotation. No loss of gouge is observed during our experiments down to the residual shear stress as long as the measured gouge thickness does not decrease. Note that water vapor can escape from the simulated fault system in-between the Teflon sleeve and rock cylinders during experiments [*Hirose and Bystricky*, 2007; *Boutareaud et al.*, 2008]. An initial pre-run load includes manual clockwise and counterclockwise $\pi/4$ rotations of the rotating cylinder to consolidate the gouge under the same normal stress as during the experiment. This increases the packing density for a larger strength of the gouge. Experiments consist of less than 60 s rotary-shear tests, leading to general

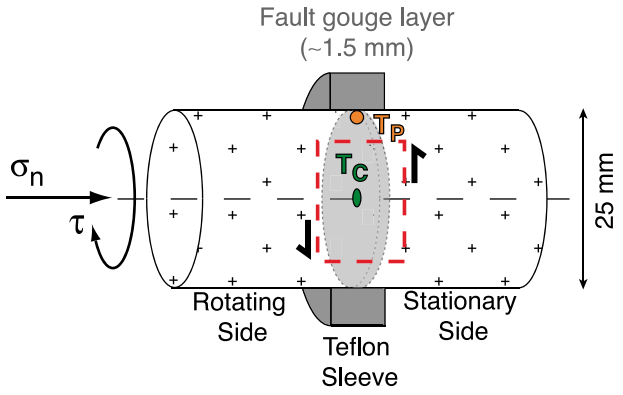

Figure 1. Schematic view of the experimental assembly. The dashed rectangle shows position of post-run thin sections. *Tp* stands for calculated peripheral temperature (orange circle), and *Tc* stands for calculated axis-center temperature (green ellipse). *Tp* and *Tc* are located at the interface of the talc gouge and the rotating cylinder.

non-coaxial shear deformation of the thin simulated fault gouge.

[9] The sample geometry implies an angular velocity increase from the center of the rotation axis to the periphery. Assuming that the shear stress τ is constant over all of the sliding surface area S, an equivalent slip velocity V_{eq} is defined such that $\tau V_{eq} S$ gives the rate of total frictional work [*Shimamoto and Tsutsumi*, 1994; *Hirose and Shimamoto*, 2005]:

$$V_{eq} = \frac{4}{3}\pi\omega R \tag{1}$$

where R is the radius of the sample and ω the angular velocity (in rad s^{-1}). The Teflon effect on shear stress is not corrected. The equivalent slip reported as "displacement" hereafter corresponds therefore to the slip at two thirds of the total radius. Twenty-three experiments have been carried out at room temperature (25°C) at a fixed rotation rate of 1500 rotations per minute, which corresponds to equivalent slip-velocities of 1.31 m s^{-1} (Table 1). The applied normal stress is fixed at 0.3 to 1.8 MPa.

[10] To monitor water vapor release by the fault during sliding in the sealed specimen chamber, a moisture sensor has been placed 20 mm away from the sliding surfaces [e.g., *Hirose and Bystricky*, 2007]. Thermal expansion of the two cylinders along the revolution axis by rapid frictional heating has already been calculated to be negligible compared to the measured fault gouge thickness [*Boutareaud et al.*, 2008]. Therefore, positive or negative value of the measured fault thickness reflects either gouge dilatancy or compaction, respectively (Figure 2).

[11] Gouge porosity measurements are made from SEM images for a wide range of magnification, and named *estimated* porosity hereafter (for procedure, see section 3.2.1). *Estimated* porosity is then compared to the *dynamic porosity* calculated from the dynamic bulk volume change of the simulated fault, which is calculated from the fault gouge thickness.

[12] Two types of SEM apparatuses have been used: a FEI Quanta 200FEG, equipped with Ametek-EDAX Pegasus analytical system including Sapphire Si(Li) detector and a Zeiss Ultra, using QBSD detector for high-kV backscattered electron contrast at 15 kV accelerating voltage for SEM images. TEM cross-sections have been obtained from a focus ion beam (FIB-SEM) apparatus: a Zeiss NVision40, using EsB detector for low-kV backscattered electron contrast at 3 kV accelerating voltage for SEM images. TEM observations have been conducted on a FEI Tecnai G2 under an acceleration voltage of 200 kV.

2.3. Temperature Calculation

[13] In order to evaluate temperature rise during the experiments, we numerically solved the heat equation taking into account the heat production and heat diffusion in the domain formed by the two cylinders and the gouge (Figure 3). Since the geometry is axisymmetric, we can restrict the computation of the temperature T only to a 2-D framework, by considering the following heat equation in a cut containing the symmetry axis:

$$\rho c_p \frac{\partial T}{\partial t} - k\Delta T = Q \tag{2}$$

where k (2) in W m^{-1} K^{-1} is the thermal conductivity, c_p (1000 for gabbro and 850 for talc) in J kg^{-1} K^{-1} is the specific heat capacity and ρ (2650 for gabbro and 2750 for talc) in kg m^{-3} is the mass density.

[14] All frictional work is assumed to be converted to heat. Heat generation rate Q (i.e., the quantity of produced heat per unit volume in unit time) is then expressed [*Noda and Shimamoto*, 2005] by

$$Q = \dot{\gamma}\tau \tag{3}$$

where $\dot{\gamma}$ is the shear-strain rate in s^{-1} and τ is the shear stress in Pa. Shear-strain rate is defined as

$$\dot{\gamma} = \frac{V}{w} \tag{4}$$

where V is the slip-rate (proportional to the radial position) in m s^{-1} and w (30×10^{-6} m for #1472 and 40×10^{-6} m for #1475) is the width of deformation zone in m. Considering that all the deformation is localized in a narrow portion of the fault zone volume (named Principal Slip Zone or PSZ hereafter), the heat source (Q) is proportional to the shear stress and to the radial position.

[15] To solve the heat equation (2), a numerical code based on the finite element method (SETMP software) has been used [*Calugaru et al.*, 2003; *Boutareaud et al.*, 2008]. It uses a finite element of the second order for a good accuracy and the iterative gradient conjugate method with Symmetric Successive Over Relaxation (SSOR) preconditioner [*Saad*, 2003] to solve algebraic systems with a fast convergence.

[16] In order to minimize the calculation duration, talc friction at coseismic velocities is assumed to approximately follow the empirical slip-weakening equation [*Mizoguchi et al.*, 2006]:

$$\tau_d = \tau_{ss} + (\tau_p - \tau_{ss}) \times \exp\left(\frac{\ln(0.05) \times d}{D_c}\right) \tag{5}$$

Table 1. Summary of the Principal Parameters for All Conducted High-Velocity Experiments[a]

Run	Humid Conditions	Initial Peak			Steady State			Slip-Weakening Distance (m)	Total Displacement (m)	Amount of Stress Drop (MPa)	Maximum Dilatancy (mm)	Equivalent Slip-Velocity (m s^{-1})	Total Fracture Energy (MJ m^{-2}) at Dc	Frictional Heat (MJ m^{-2}) at Dc	Dissipated Energy (MJ m^{-2}) at Dc
		Shear Stress (MPa)	Normal Stress (MPa)	Power Density (MPa^{-2} m s^{-1})	Shear Stress (MPa)	Normal Stress (MPa)	Power Density (MPa^{-2} m s^{-1})								
#1472	Dry	0.77	0.95	0.85	0.21	1.02	0.73	19.49	42.49	0.57	0.34	1.31	5.52	4.06	9.58
#1473	Dry	0.97	1.36	0.41	0.27	1.48	0.35	15.72	36.54	0.70	0.56	1.31	5.52	4.19	9.70
#1474	Dry	0.54	0.55	2.53	0.16	0.62	1.97	24.33	42.84	0.38	0.14	1.31	4.58	3.99	8.57
#1587	Dry	0.46	0.27	10.47	0.12	0.37	5.58	37.69	49.19	0.34	0.07	1.31	4.52	4.52	9.05
#1588	Dry	1.17	1.80	0.24	0.32	1.86	0.22	10.70	23.67	0.85	0.62	1.31	3.42	3.42	6.85
#1478	Dry	0.75	0.96	0.83	0.62	1.06	0.68	-	2.00	-	-	1.31	0.10	0.96	1.07
#1479	Dry	0.73	0.95	0.84	0.58	1.06	0.67	-	2.99	-	-	1.31	0.19	1.43	1.63
#1480	Dry	0.73	0.96	0.83	0.53	1.06	0.67	-	4.71	-	-	1.31	0.28	1.52	1.80
#1481	Dry	0.74	0.97	0.81	0.40	1.04	0.71	-	7.36	-	-	1.31	-	-	-
#1482	Dry	0.73	0.95	0.84	0.24	1.05	0.70	-	15.25	0.49	0.22	1.31	-	-	-
#1585	Dry	0.84	0.96	0.83	0.48	1.06	0.68	-	7.44	-	-	1.31	4.26	-	-
#1586	Dry	0.80	0.97	0.81	0.31	1.05	0.69	-	16.44	0.49	0.42	1.31	-	9.57	-
#1714	Dry	0.71	0.97	0.82	0.22	1.11	0.62	23.67	40.68	0.49	0.44	1.31	5.85	5.14	10.99
#2290	Dry	0.67	1.00	-	-	-	-	-	31.40	-	-	1.31	-	-	-
#1475	Wet	0.50	0.97	0.81	0.15	1.03	0.72	3.72	33.67	0.35	-	1.31	0.65	0.55	1.20
#1476	Wet	0.29	0.55	2.50	0.13	0.59	2.20	0.37	33.18	0.16	-	1.31	0.03	0.05	0.08
#1477	Wet	0.52	1.37	0.41	0.14	1.44	0.37	6.06	24.07	0.38	-	1.31	1.16	0.83	1.99
#1589	Wet	0.24	0.60	2.12	0.08	0.70	1.56	-	38.01	0.16	-	1.31	-	-	-
#1590	Wet	0.24	0.25	12.21	0.12	0.33	7.01	60.87	49.47	0.12	-	1.31	3.65	7.30	10.96
#1592	Wet	0.44	1.78	0.24	0.14	1.73	0.26	0.38	27.89	0.30	-	1.31	-	-	-
#1483	Wet	0.35	0.97	0.82	0.17	1.01	0.75	1.59	5.68	0.17	-	1.31	0.14	0.27	0.41
#1484	Wet	0.37	0.98	0.79	0.18	1.00	0.76	0.36	11.61	0.19	-	1.31	0.03	0.07	0.10
#1715	Wet	0.32	0.97	0.81	0.08	0.98	0.80	0.05	26.42	0.24	-	1.31	0.01	0.004	0.01

[a]The *total fracture energy* is the area under the slip-weakening curve, between the peak shear stress and the residual shear stress. The *frictional heat* is the work of the residual shear stress. The *dissipated energy* is the total mechanical energy (i.e. the sum of the *total fracture energy* and the *frictional heat*).

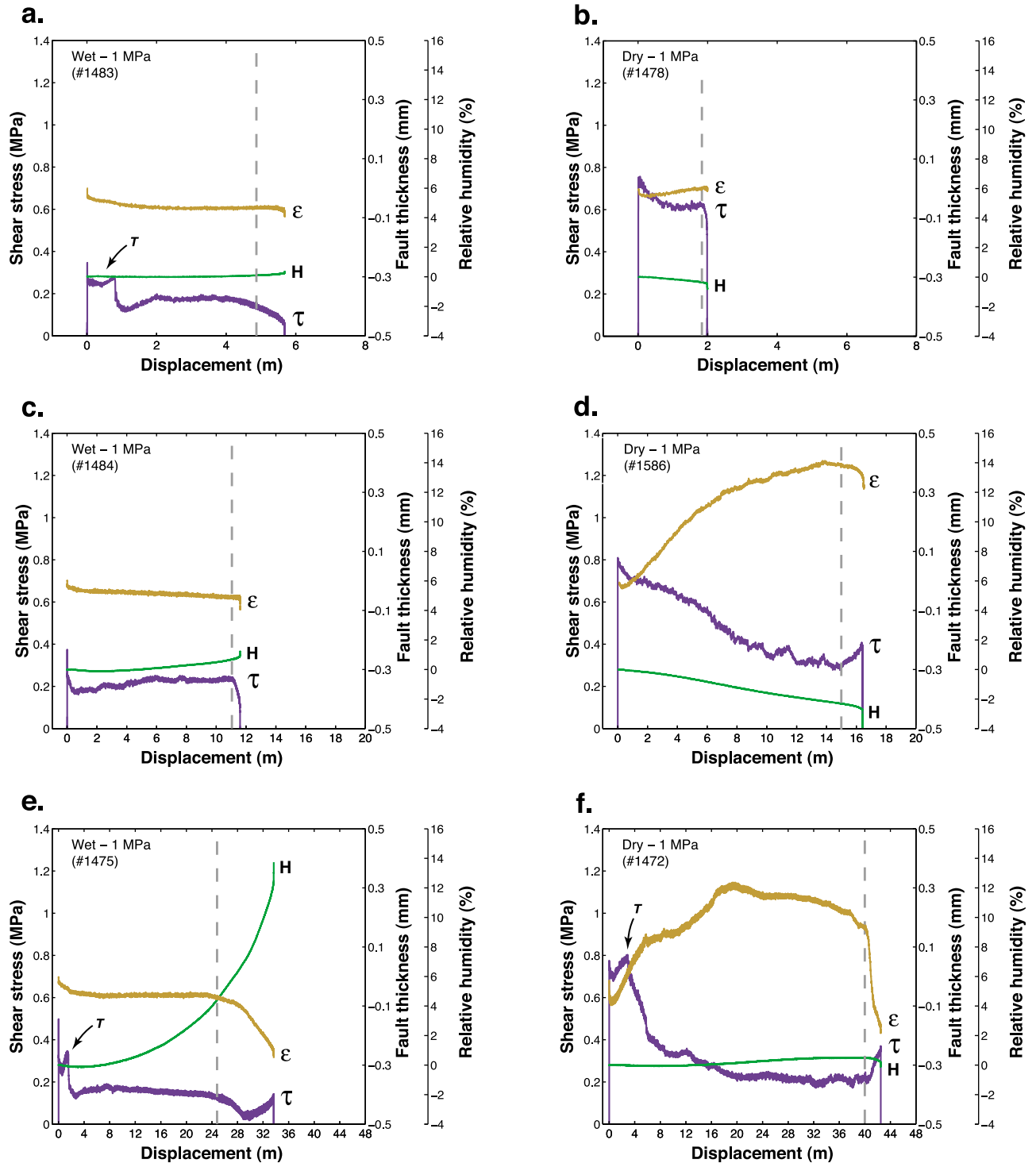

Figure 2. Representative fault shear stress (τ), the fault thickness (ε), and the relative humidity (H) in the sealed chamber containing the fault, versus displacement at velocity of 1.31 m s^{-1}, for wet and dry conditions. (T) stands for Teflon effect. The vertical gray dashed line indicates the arrest of the high-speed rotary-shear motor. (left) Wet conditions, (right) dry conditions. Experiments have been stopped at several different displacements: (a) 6 m, (b) 2 m, (c) 12 m, (d) 16 m, (e) 34 m and (f) 42 m.

where τ_d is the instantaneous dynamic shear stress in Pa, τ_{ss} is the residual (steady state) shear stress in Pa, τ_p is the peak shear stress in Pa, d is the displacement and D_c is the slip-weakening distance in m necessary for the fault to reach the residual shear stress. D_c is determined by fitting equation (5) to the experimental data by the least squares method.

[17] The numerical model has been validated for wet and dry experiments, by comparing the calculated temperature from four thermocouples located in the stationary cylinder

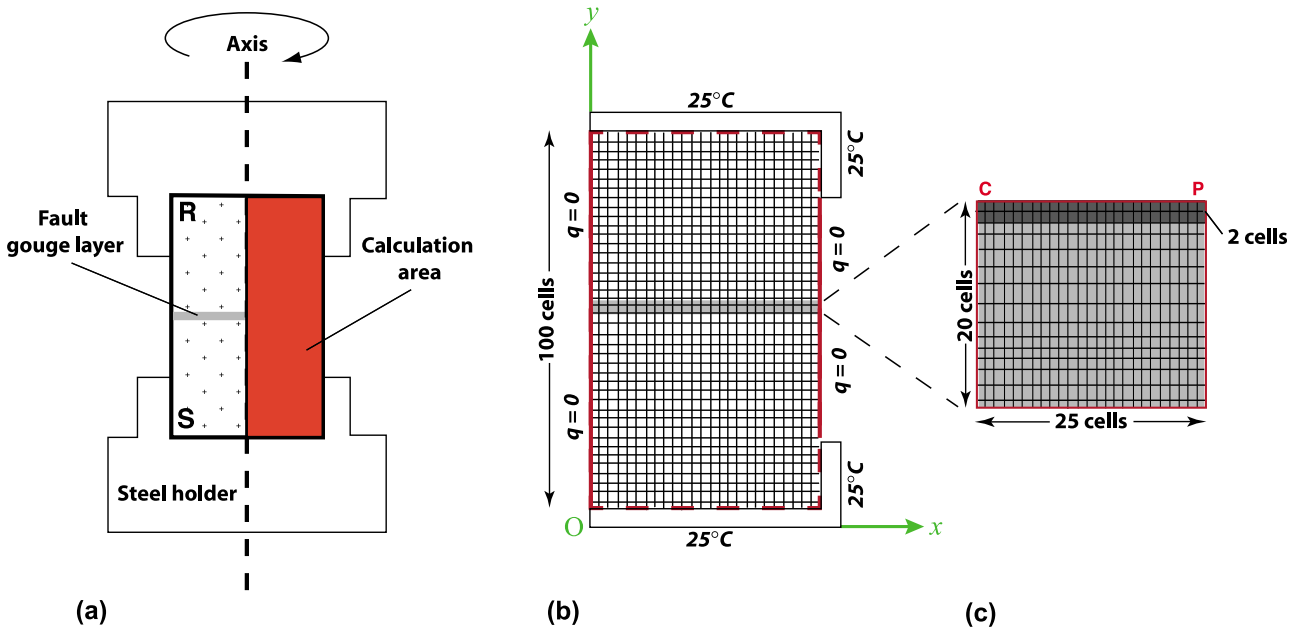

Figure 3. Sketch of the gouge-gabbro system used for numerical simulation. (a) Geometry of the specimen sample. *R* means rotary side and *S* means stationary side. (b) Enlarged sketch of the total calculation domain showing assumed boundary conditions. The light gray central part represents the gouge zone. (c) Enlarged sketch of the heat production gouge zone. The dark gray zone represents the PSZ. Only 20 by 50 cells are used to calculate the heat generation rate. *C* means central part of the heat production zone (axis-center of the cylinder where *Tc* is calculated), and *P* means peripheral part of the heat production zone (periphery of the cylinder where *Tp* is calculated).

set at different distances (1, 5, 10 and 15 mm) from the fault surface (#1714 and #1715) [*Boutareaud et al.*, 2009]. For the thermocouple closer to the fault surface, a maximum difference from calculated temperature of ±5°C for the first 11 m of displacement, and +30°C subsequently has been observed in wet conditions. The deviation between calculation and measurement could be probably related to the limits of the considered physical model that assumes that cylinders and gouge are solid media (not porous media) and therefore it is not able to take into account some phenomena (as the phase change of water), which could be significant.

[18] To account for the radial distribution of temperature that results from the variation in slip-velocity, the reported calculated temperatures (Figure 4) consider only two points located closely at the interface of the talc gouge and the rotating cylinder: one at the axis-center of the cylinder (*Tc*) and the other at the periphery of the cylinder (*Tp*).

3. Results

3.1. Evolution of Physical Parameters During Experiments

[19] The first-order trend of our friction experiments appears to be reproducible. It exhibits an exponential decay in fault strength from a peak value (τ_p) to a steady state (i.e., residuals shear stress) value (τ_{ss}) over a slip-weakening distance (D_c). Empirical laws can fit this slip-weakening behavior. The version in best agreement with experimental data is expressed in equation (5). In this equation (see Figure 5 for definitions), D_c represents the post-peak distance necessary to achieve 95% of the total weakening [*Mizoguchi*

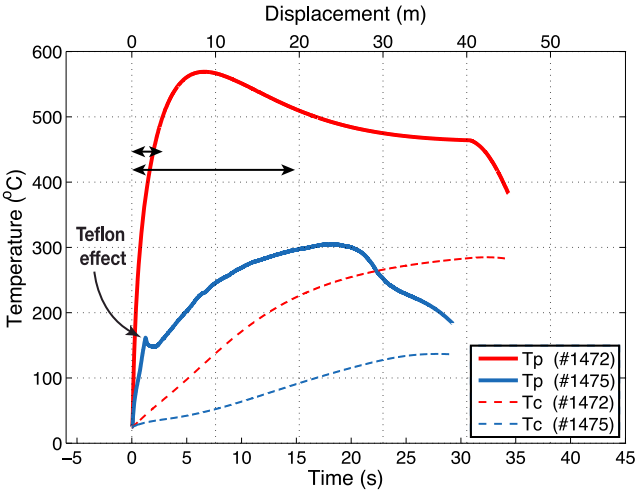

Figure 4. Calculated temperature evolution versus time for two representative experiments conducted at 1.31 m s^{-1} and 1 MPa normal stress. Red color corresponds to the dry experiment (#1472), and blue corresponds to the wet experiment (#1475). Plain lines stand for peripheral assembly temperatures (*Tp*), and dashed lines stand for central assembly temperatures (*Tc*). Long-length and short-length arrows indicate the slip-weakening duration for #1472 and #1475, respectively. The right ends of the arrows point out the slip-weakening distance necessary for the simulated faults to reach the residual shear stress.

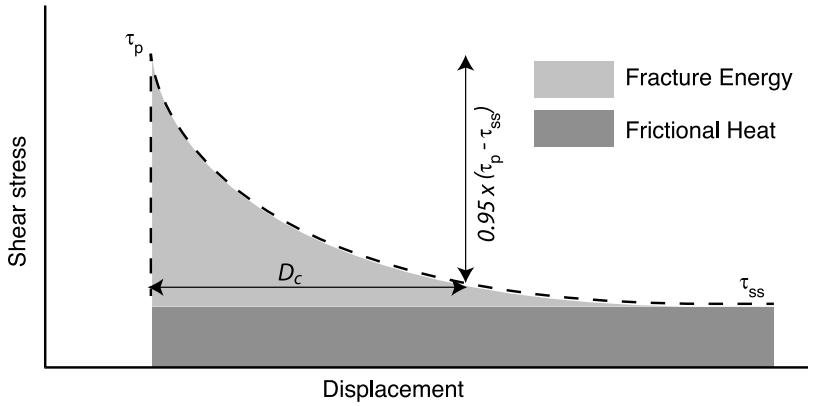

Figure 5. Schematic diagram showing the significance of the various parameters used in the empirical equation (5) to fit the weakening behavior of simulated faults at high slip-velocity.

et al., 2007a]. Two additional parameters have been calculated: the dissipative energy and the power density. The dissipative energy represents the total work per unit fault area. It refers to the summation of the total fracture energy per unit area (i.e., the area under the slip-weakening curve) equals to as $0.5*(\tau_p - \tau_{ss})*D_c$, and the frictional heat per unit area (i.e., the work of the residual shear stress) calculated as $\tau_{ss}*D_c$. The power density represents the energy exchanged on the sliding surface per unit time and unit area. It is equal to $1/(\tau.V)^2$.

[20] A summary of experimental conditions and slip-weakening physical parameters is given for each test in Table 1. Our talc friction experiments have been conducted from 0.3 to 1.8 MPa of normal stress (see Table 1). Peak shear stress values range from 0.46 to 1.17 MPa for dry conditions, and from 0.24 to 0.52 MPa for wet conditions. Residual shear stress values range from 0.12 to 0.62 MPa for dry conditions, and from 0.08 to 0.18 MPa for wet conditions. Stress drop values range from 0.12 to 0.38 MPa for wet conditions, and from 0.34 to 0.85 MPa for dry conditions. Slip-weakening distance values D_c range from 0.05 to 60.87 m for wet conditions, and from 10.70 to 37.69 m for dry conditions. During these experiments, the torsion motor is suddenly stopped (the deceleration occurs over about few millimeters of displacement). The random increase in shears stress at the end of the experiments is due to a slight leak of gouge.

[21] Second-order trends of our friction experiments occasionally show a second peak of friction that can be preceded by a plateau and followed by a second weakening (i.e., Figure 2). Video monitoring of the sample assembly show the Teflon sleeve moving away from its initial position, which tends to impede revolution of the rotating cylinder. This problem originates from a self-adjustment of a slight misalignment of the Teflon sleeve relatively to the rotating rock cylinder (see *Sawai et al.* [2012] for a complete review on Teflon artifacts for this experimental setting). Accordingly, the second peak of friction is interpreted as an experimental artifact. It is important to note that the first-order of the mechanical behavior of the simulated faults remains independent of this experimental artifact (Figure 2).

[22] Only wet tests show a release of water (for a displacement higher than 8 m) with a relative increase of humidity in the range of $8 \pm 2\%$ once motor is stopped. This indicates that enough heat is produced by friction to allow water phase transition from liquid to vapor. However, because our simulated fault is sealed by a Teflon sleeve, the amount of released water is directly attributed to the degree of fault sealing or sleeve movement. The negative values of humidity percentage observed in the first few meters on Figure 2 can be reasonably explained by the increase of fault temperature, leading to a small change of vapor water pressure in the vicinity of the moisture sensor. For these two reasons, the absolute measured value of humidity cannot be accurately established.

[23] The slip-weakening distance D_c represents the amount of displacement necessary for the dynamic fault shear stress to achieve 95% of the weakening from the peak shear stress to the residual shear stress. In the following, for convenience, D_c is assimilated to the distance value of the slip-weakening.

[24] The observed compaction at the beginning of all runs is usual for this type of experiments, leading to a porosity reduction and gouge consolidation [see *Boutareaud*, 2007], with contact-junction strengthening by increasing the quality of contacts between sliding surfaces [*Rice et al.*, 2001]. From the measured fault thickness changes, we have calculated the relative gouge porosity variations for dry tests, for an estimated standard deviation of $\pm 2.4\%$. Dry tests show a compaction of the gouge of 4% at about 0.5 m of displacement, which progressively decreases up to $\sim$1.5 m where compaction changes to dilation (e.g., Figure 2f). From there, gouge dilatancy exponentially increases up by $\sim$23% until the fault reaches the residual shear stress at D_c. Then, the fault returns to the initial porosity by compaction.

[25] For the sake of clarity, we report only data from 1 MPa normal stress experiments in this paragraph, thus the reported shear stresses equal the friction coefficient, μ. The calculated temperature evolution of experiments #1472 and #1475 (Figure 4) shows an exponential increase of *Tp* for dry and wet conditions. A peak value of 569°C and 304°C is reached after around 6 s (equivalent to 8 m of displacement) and 17s (equivalent to 22 m of displacement), respectively. At D_c (see Table 1), the *Tp* temperature is around 512°C for dry conditions, and around 160°C for wet conditions. On the contrary, *Tc* increase remains logarithmic during the duration of the experiments. It reaches a maximum value of 113°C and 101°C at 6s and 17 s for dry and wet experiments,

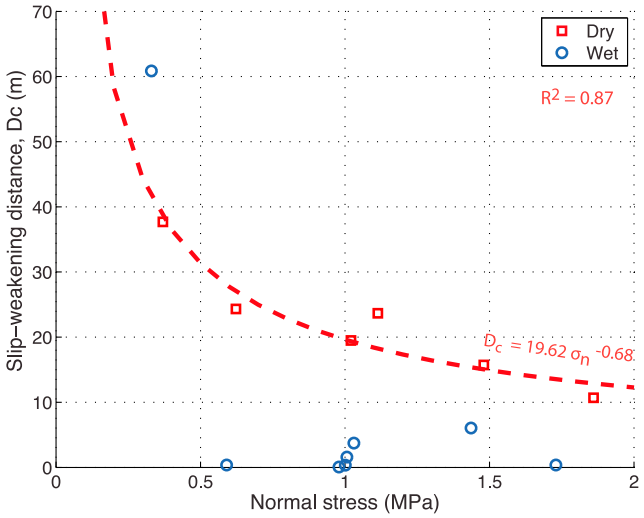

Figure 6. Slip-weakening distance (D_c) versus normal stress. Dry experiments show a decrease in power law of D_c with increasing normal stress. No reasonable fit can be obtained for wet conditions. Wet values are lower than dry values.

respectively. At D_c (see Table 1), the maximum reached *Tc* temperature is 228°C and 36°C for dry and wet experiments, respectively.

[26] From the measured primary fault physical parameters, we were able to investigate the fault mechanical behavior of talc at seismic slip-velocities for a limited number of relationships:

[27] 1. D_c exhibits a negative dependence in power law on applied normal stress, for dry conditions (Figure 6). No evident relation could be found for wet conditions.

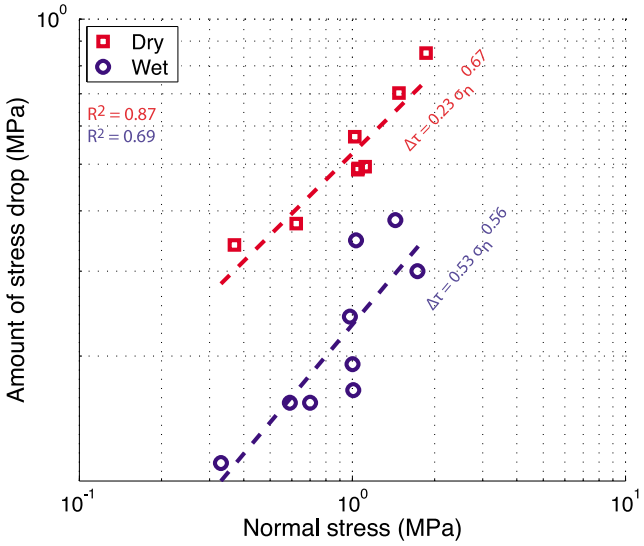

Figure 7. Amount of stress drop versus applied normal stress. The amount of stress drop is always higher in dry conditions compared to wet conditions. In best fit equations, $\Delta\tau$ stands for amount of stress drop.

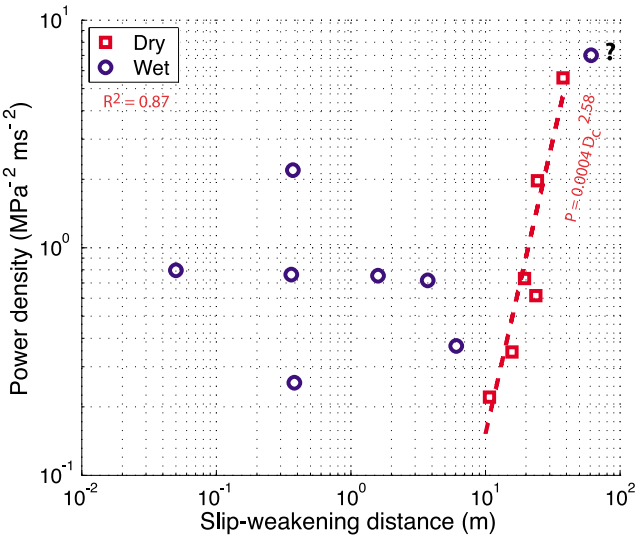

Figure 8. Fault power density at the residual state versus slip-weakening distance (D_c). In best fit equation, P stands for power density. Question mark indicates that the relevance of the point needs to be investigated. There is no apparent correlation for dry conditions.

[28] 2. Dynamic stress drop shows a positive power law dependence on applied normal stress for dry and wet conditions (Figure 7).

[29] 3. The experimental data set shows that fault power density strongly increases with D_c for dry conditions only (Figure 8). In wet conditions, the general trend does not show any dependence of fault power density on D_c.

[30] 4. The measured maximum gouge layer dilation is directly proportional to the applied normal stress, in dry conditions only (Figure 9).

[31] The relevance of these experimental data is discussed in section 4.4.

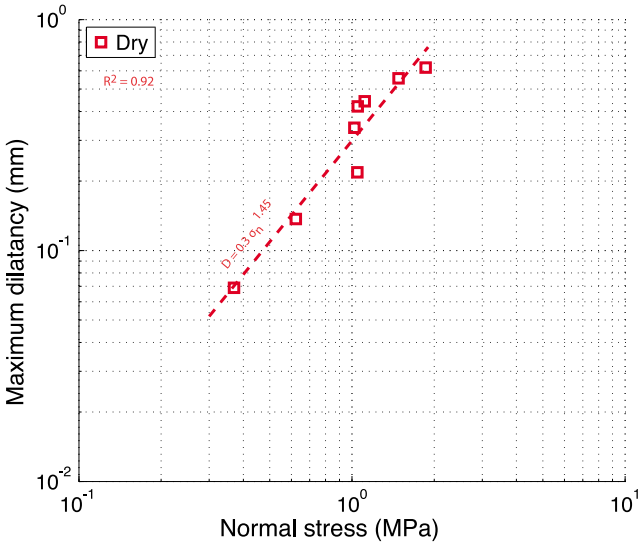

Figure 9. Fault maximum dilatancy versus applied normal stress. In best fit equation, D stands for maximum dilatancy.

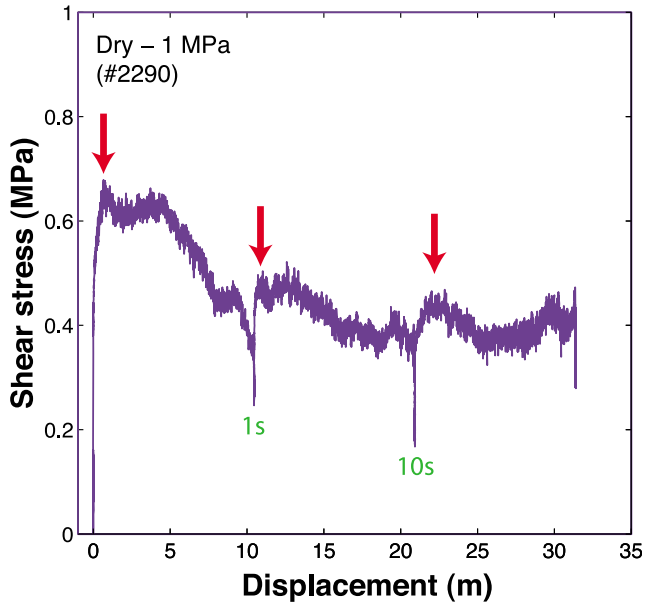

Figure 10. Evolution of shear stress as a function of displacement for two hold times from slide-hold-slide tests. Experiment has been conducted at 1.31 m s^{-1} for dry conditions. Red arrows indicate peak shear stress for each slip cycle. Green numbers indicate holding time.

[32] A representative slide-hold-slide experiment is also reported for dry conditions (Figure 10). Slip-velocity and normal stress were maintained constant at 1.31 m s^{-1} and 1 MPa, respectively. During this experiment, the torsion motor was gradually stopped (the deceleration occurs over about one meter of displacement) once an apparent steady state level of shear stress was reached. This corresponds to a hold. Hold times stand for few seconds and then, the motor was started again. Three strain-cycles are then defined. The simulated fault exhibits a slip-weakening behavior, with a higher slope for the first cycle. The shear stress evolves from a peak value of 0.67 to a steady state value of 0.44 MPa for the first strain-cycle, from 0.50 to 0.39 MPa for the second strain-cycle, and then from 0.47 to 0.37 MPa for the third strain-cycle.

3.2. Microstructures

3.2.1. Procedures and Methods for Image Analysis

[33] Experiments were stopped at different stages of slip-weakening behavior. Microstructures therefore correspond to finite strain. In order to observe intelligible microstructures, thin sections have been made at about 4 mm from the external cylindrical surface, perpendicular to the gouge layer and nearly parallel to the slip direction. A set of extra thin sections has been made through the axis-center of the assembly to complete observations.

[34] We analyzed shape-preferred orientations (SPO) of talc clasts (≥20 μm) using the PAROR method [*Panozzo*, 1983]. Remaining part of the images (talc clasts ≤20 μm for which a shape is hardly definable at the used magnification) is considered to be the matrix and cracks are avoided. Image analysis has been carried out with public domain MATLAB toolbox PolyLX [*Lexa*, 2003] (http://petrol.natur.cuni.cz/~ondro/polylx:home) and ImageSXM [*Barrett*, 2002] (http://www.liv.ac.uk/~sdb/ImageSXM). We have divided the analyzed fault shear zones into three domains in order to observe spatial SPO variations. Boundary domains 1 and 3 were chosen arbitrarily at 18% of the gouge thickness and domain 2 comprises the remaining central 64%. The purpose of such distinctive analysis is to obtain SPO variations in the central part of the gouge, further away from any possible influence of the boundary domains. For comparison a bulk SPO is also calculated for every analyzed picture using clasts from all three domains (Figure 11). Clast-to-matrix ratio quantifies the amount of comminution and is calculated as the area fraction of talc clasts (≥20 μm) divided by the area fraction of clasts and matrix. It spans from 1 (analyzed area is formed entirely of talc clasts) to 0 (analyzed area is formed entirely of matrix; see *Pec et al.* [2012]).

3.2.2. Optical Microscope and SEM Observations

[35] Hereinafter, for the sake of clarity, we only report the results of 6 representative experiments conducted at 1 MPa normal stress. The progressive development of microstructures (i.e., fabrics, clast-to-matrix ratio, SPO and porosity) is then reported at 6, 12 and 34 m of displacement for wet conditions, and at 2, 16 and 42 m of displacement for dry conditions (i.e., at the early/late stage of the slip-weakening, and at the frictional steady state). At 34 and 42 m of displacement, the residual shear stress is achieved in both cases.

[36] Pre-run fault gouge exhibits a weak SPO synthetic with the induced sense of shear (Figures 11a and 11b). The clast-to-matrix ratio is ~0.25 and is constant through the whole gouge layer. *Estimated* gouge porosity (error of ±2.5%) is about 20% for both wet and dry conditions.

[37] Irrespective of humidity conditions and displacement, a continuous and pervasive layer of platy grains with a strong SPO synthetic with the induced sense of shear can be observed lying immediately next to the gouge/cylinder interface. In wet conditions, this fabric consists of a complex array of variably anastomosing shear planes with a S-C or S-C-C′ structure (scaly fabric; Figure 12c). In dry conditions, this fabric consists exclusively of planes parallel to the C- direction (Figure 12d). The pervasive layer is named Principal Slip Zone (or PSZ). Whatever humidity conditions, these grains show a pervasive interlayer delamination. The PSZ *estimated* porosity is 9% for wet conditions, and around 3% for dry conditions. Increasing displacement to about 15 m can lead locally to a small increase of the PSZ thickness up to 50 μm as an average, and exceptionally 150 μm as a maximum.

[38] In wet experiments, talc clasts develop a strong SPO parallel (±3.5°) to the C-shear direction already after 6 m of slip and retain this orientation with increasing displacement up to 34 m (Figures 11c, 11e and 11g). The strength of the SPO is independent on the amount of displacement. Some grains have a (001) preferred orientation parallel to an incipient S-foliation at 30° with respect to shear direction. The fine-grained matrix is mainly composed of thin platy grains. This matrix surrounds larger platy grains (Figure 12a). Some of these grains show significant interlayer delamination. Few platy subrounded grains can also be observed for all three steps (6, 12 and 34 m). The clast-to-matrix ratio remains unchanged (within the error of image analysis) compared to the starting material and is independent on the amount of displacement as well. *Estimated* gouge porosity in the central part at ~2–~15 m of displacement remains around 10%, but

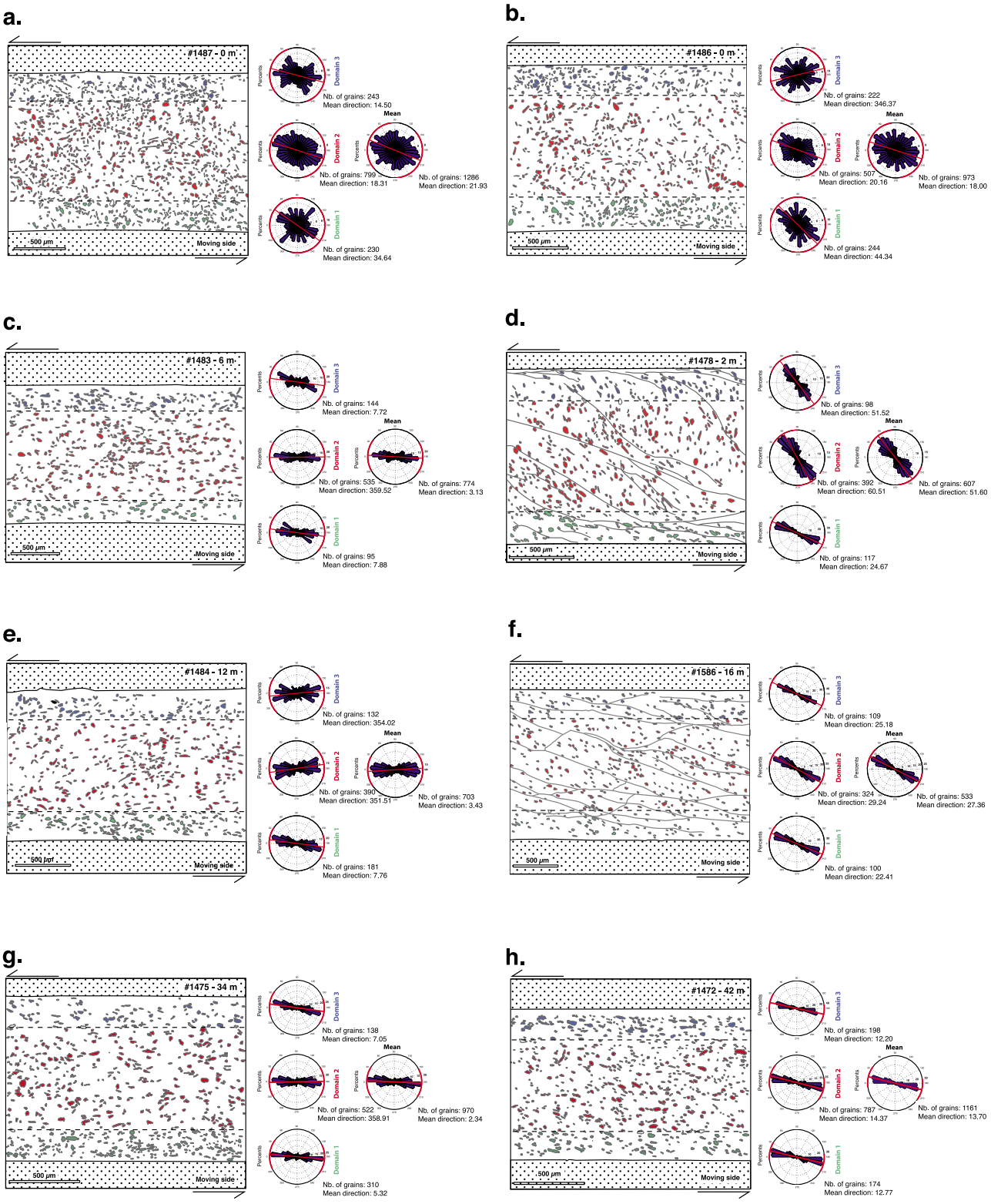

Figure 11. Two-dimensional analysis of talc grain shape preferred orientation based on post-run fault SEM images. Only talc grains with a long axis ≥20 μm are here considered. A rose diagram is used to represent the different orientation distribution in percent for three different gouge domains. Not all analyzed grains are shown. The color code corresponds to assigned domain. Left column – wet conditions, right column – dry conditions. (a) Initial state in wet conditions, (b) initial state in dry conditions, (c) at 6 m in wet conditions, (d) at 2 m in dry conditions, (e) at 12 m in wet conditions, (f) at 16 m in dry conditions, (g) at 34 m in wet conditions, and (h) at 42 m in dry conditions.

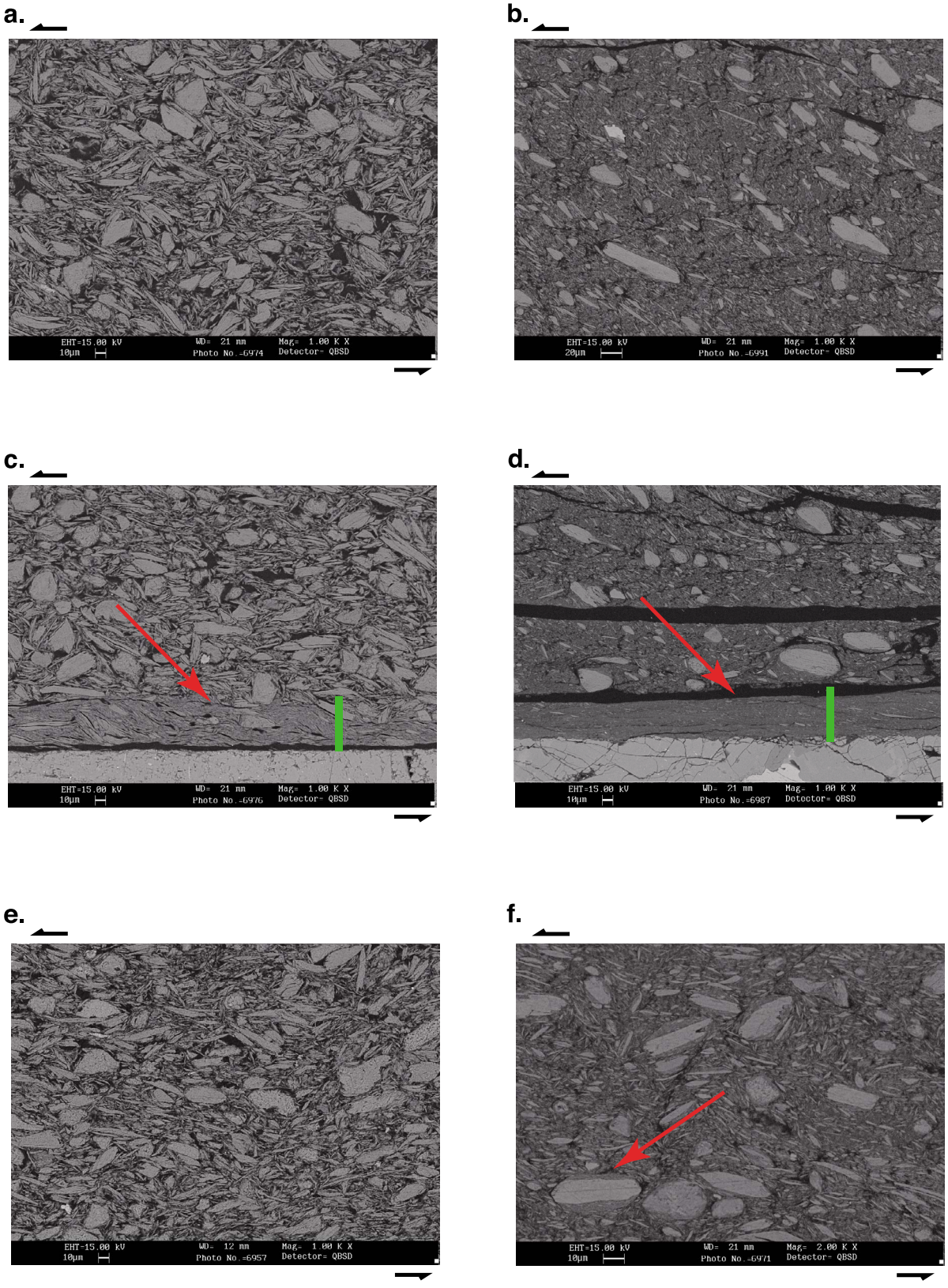

Figure 12. SEM photomicrographs (backscattered electron contrast at 15 kV) of post-run fault gouges for wet (left side) and dry (right side) conditions. Sense of shear is top to the left. (a, b) Central gouge for #1484 (12 m) and #1586 (16 m), respectively. (c, d) Principal Slip Zone indicated by a red arrow for the same samples #1484 and #1586, respectively. The green vertical segments locate position of PIPS sections done for TEM. (e, f) Central gouge for #1475 (34 m) and #1472 (42 m), respectively. A red arrow indicates a grain showing a cortex of irregular and non-concentric fine-grained aggregated material.

drops to ~5% after 34 m of displacement (Figure 12e). This is consistent with the 15% and 1% of *dynamic porosity* for ~2–~15 m and 34 m of displacement, respectively.

[39] Dry experiments show more complicated microstructures. After 2 m of displacement (Figure 11d), we observe the development of open S-oriented shear planes crosscutting the central gouge (i.e., remaining part of the gouge layer that is not the PSZ) with a mean orientation of 29° with respect to shear direction. In the central part of the gouge (domain 2) a stacking arrangement of sigmoidal mm-thick lenses (up to 3.65x0.50 mm) in a C-S structure is observed (Figure 11e). These lenses link the two gouge/cylinder interfaces, frequently branching off from a single C-oriented shear plane laying at around 180 μm from the rotating cylinder. After 16 m of displacement (Figure 11f), we observe S-, C- and rare C′-oriented shear planes crosscutting the fault shear zone. The SPO further strengthens and the mean orientation of clasts (27°) doesn't show significant variations between domains. The abundant very fine-grained matrix is mainly composed of thin platy grains. This matrix surrounds larger platy subangular to subrounded grains (Figure 12b). Some of these grains show a pervasive interlayer delamination. A striking characteristic of many of these clasts is that they are surrounded by a cortex (Figure 12f) made of nm- to μm-thick aggregated grains and show an irregular thickness ranging from 0.5 to 5 μm. This cortex does not show a concentric arrangement. The clast-to-matrix ratio further decreases from ~0.18 down to ~0.11. *Estimated* gouge porosity in the central part remains around 10%, which is lower than the 36% of *dynamic* porosity calculated at 16 m of displacement. Finally, at 42 m of displacement in dry gouge experiments, we observe a strong SPO in the central part of the fault gouge with most of grains that are at low angle to the (C-) shear direction (0° to 30°, 14° as a mean orientation, Figure 11h). Open C-S shear planes have disappeared. The abundant very fine-grained matrix is mainly composed of thin platy grains. This matrix surrounds larger platy subangular to subrounded grains. Some of these grains show significant interlayer delamination. Few platy subrounded grains can also be observed. Again, as for 16 m of displacement, many of these grains are surrounded by an irregular 0.5 to 5 μm-thick cortex of nm- to μm-thick aggregated grains without any concentric arrangement. The clast-to-matrix ratio does not change any further compared to 16 m of displacement. *Estimated* gouge porosity in the central part is around 4%, which is much lower than the 25% of *dynamic* porosity.

[40] Energy Dispersive X-ray Spectrometry (EDX-SEM) conducted on the grains of the central gouge and PSZ displays a high relative atomic density of O, Fe, Si and Mg elements. Additionally, detailed investigations by microscope, SEM and Raman spectroscopy do not clearly show any mineral reaction product such as enstatite or amorphous silica. This work suggests that post-run sheared gouge essentially consists of talc.

3.2.3. SEM and TEM Observations

[41] At 34 and 42 m of displacement, the residual shear stress is achieved for both wet and dry experiments (Figure 2). Detailed examination of post-experiment gouge layers by EDX-SEM element mapping does not display higher relative atomic density of any element. In the central part of the gouge, talc grains are slightly too highly delaminated along the (001) cleavage planes. They show a preferred orientation with long axis parallel to the shear direction and sheet plane parallel to the shear plane irrespective of humidity conditions (see section 3.2.2). However, detailed investigation by TEM combined to SEM show contrasting fabrics for the wet and dry experiments (Figure 12).

[42] Under dry conditions, talc interlayer delamination produces down to 20 nm-thick and down to 100 nm-long well-crystallized sublamellae in the central gouge (Figure 13a). Aggregates ranging from 50 to 200 nm in diameter, similar to the Clast-Cortex Aggregates [e.g., *Smith et al.*, 2011], can be observed (Figure 13b). These nanometric aggregates are not constituted by a nucleus surrounded by a cortex, but are constituted by a concentric arrangement of talc sublamellae (Figure 13c). EDX-SEM analysis indicates that these aggregates have the same chemical composition as the talc. These nanometric aggregates are commonly found to be together with or flattened between two talc lamellae suggesting shearing, which gives them an apparent soft aspect (Figure 13d).

[43] A striking characteristic of the central gouge and the PSZ is the non-regularly spaced alternance of stacked talc lamellae and porous zones (Figures 13a and 14a). In the PSZ, the relative proportion of porous zones is higher. Associated talc lamellae tend to be thinner (i.e. <100 nm) than in the rest of the gouge. This is in accordance with the grain comminution observed at the thin section scale (see section 3.2.2). Detailed examination of the porous zones indicates that they are composed of aggregates ranging from 50 to 300 nm in diameter (Figure 14a). These nanometric aggregates are constituted by a nucleus surrounded by a concentric arrangement of tens of talc sublamellae. The nucleus consists of one to three 10 nm-diameter subaggregates. Lattice fringes (corresponding to the 9 Å-spaced (001) planes) give evidence of the crystallinity of the talc sublamellae forming the nanometric aggregates (Figure 14b). These nanometric aggregates are commonly found in porous zones. They exhibit a nearly perfect sphere-shape suggesting they were packed loosely enough and dispersed during experiment to avoid intense grain contact and consecutive comminution [e.g., *Boutareaud et al.*, 2008]. This gives them an apparent rigid aspect (Figure 14c). Kinking and bending of thinned talc lamellae can be locally observed (Figure 14d).

[44] For dry conditions, 16 m of displacement corresponds to the slip-weakening distance (Figure 2). TEM investigation shows the occurrence of the nanometric aggregates, suggesting their formation before the residual shear stress is reached (Figure 15a).

[45] Under wet conditions, no nanometric aggregate could be observed within the central gouge or the PSZ (Figures 12 and 15b). The PSZ shows a homogeneous fabric, with a large number of talc lamellae and sublamellae with long axis parallel to the shear direction.

4. Interpretations and Discussion

4.1. Microstructural Development

[46] The angular shape of grains, the general decrease of the grain size with increasing displacement, the localization of deformation within the PSZ, the applied high strain rates under low pressure and temperature conditions, and the significant drop in shear stress indicate a brittle mode of deformation at the microscopic scale, whatever initial humidity

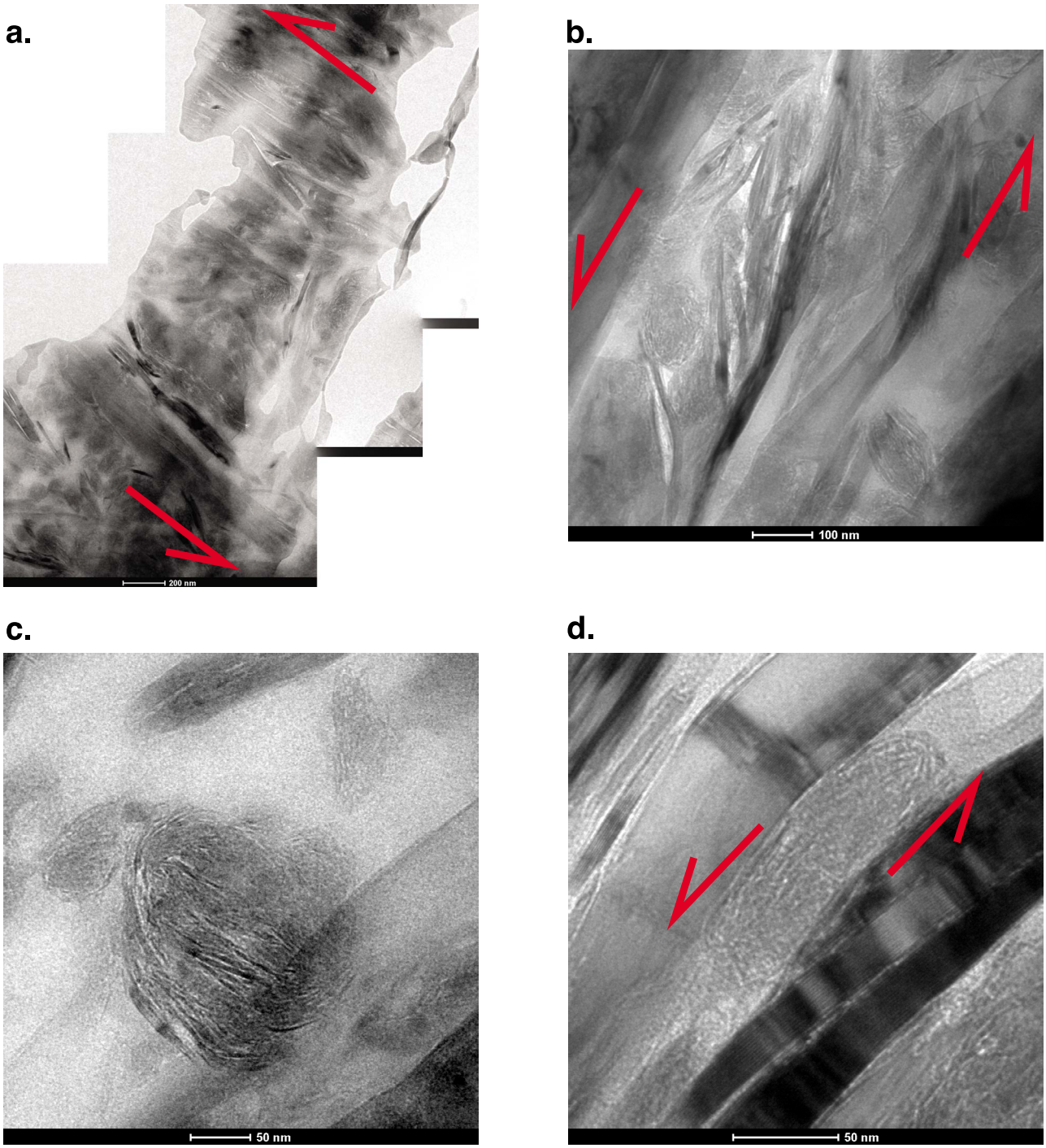

Figure 13. TEM photomicrographs from FIB sections of the central gouge for dry conditions (#1472). Sense of shear is indicated on Figures 13a, 13c, and 13d. (a) Talc lamellae and sublamellae oriented parallel to the sense of shear. (b) Higher magnification image of nanometric aggregates placed between talc lamellae and sublamellae. (c) Example of a nanometric aggregate without any nucleus. (d) Nanometric aggregate flattened between two talc lamellae.

conditions. However, at the thin section scale, the central gouge fabric shows a C-S structure, while the PSZ layer exhibits unrelated shear planes. This suggests distinct distributed deformations throughout these two units during our experiments, which is uncoupling between the central gouge and the PSZ.

[47] We attribute the difference between *estimated* and *dynamic* porosities to three issues. First, we do not take into account the open shear planes in our image analysis. Second, there is an important effect of sorting (smaller particles partially fill the gap between larger particles; e.g., Figures 12b). However, the large differences in the measured values (up to

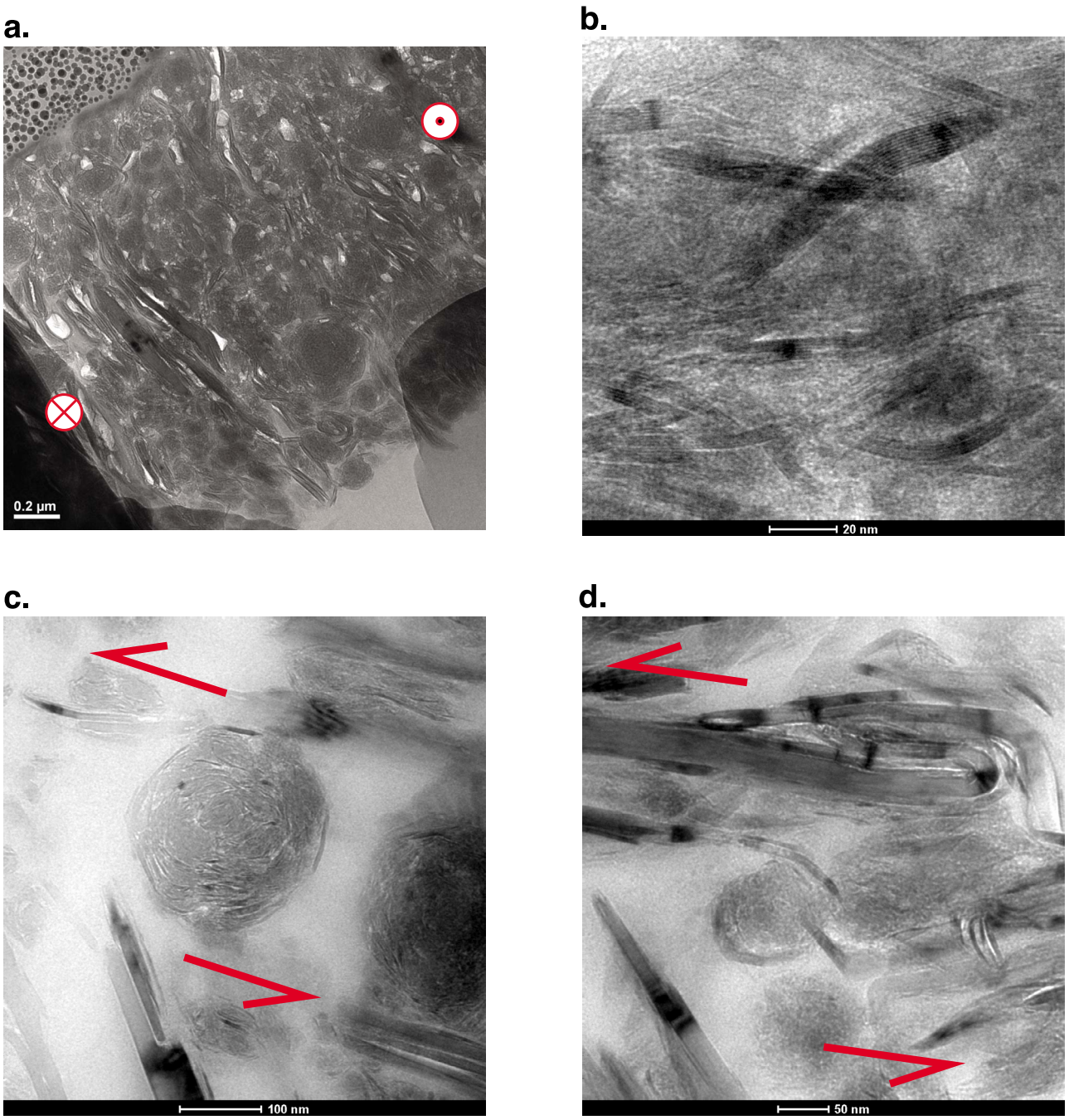

Figure 14. TEM bright field photomicrographs from FIB sections of the PSZ for dry conditions (#1472). Sense of shear is indicated on Figures 14a, 14c, and 14d. (a) Talc lamellae and sublamellae oriented parallel to the sense of shear, and nanometric aggregates. (b) Lattice fringes giving evidence of the crystallinity of the talc sublamellae forming the nanometric aggregates. (c) Example of a nanometric aggregate without nucleus. (d) Talc lamellae survivors are often bent or kinked with respect to the sense of shear.

25%) cannot be fully explained by these two issues. Rather, it seems that the *dynamic* calculated porosity is present during the experiment but collapses once the slip ceases.

[48] The SPO of grains parallel to the shearing direction observed at 6 m of displacement in wet conditions suggests a rapid reorientation of the platy grains in the first meters of displacement (Figure 11). The combination of two mechanisms can be here proposed: pure shear as first [*Grunberger et al.*, 1994; *Djéran-Maigre et al.*, 1998], and general non-coaxial shear as second. The compaction observed at the beginning of all runs, the decrease by about 10% of the central gouge porosity, and the fault zone gouge fabric is consistent with such assumption.

[49] Since post-run grains are not rounded but platy with angular to subangular edges, rolling is inhibited during shearing in the central gouge whatever initial humidity conditions [*Mair et al.*, 2002]. Thus, accommodation of fault displacement is expected to be achieved by grain sliding

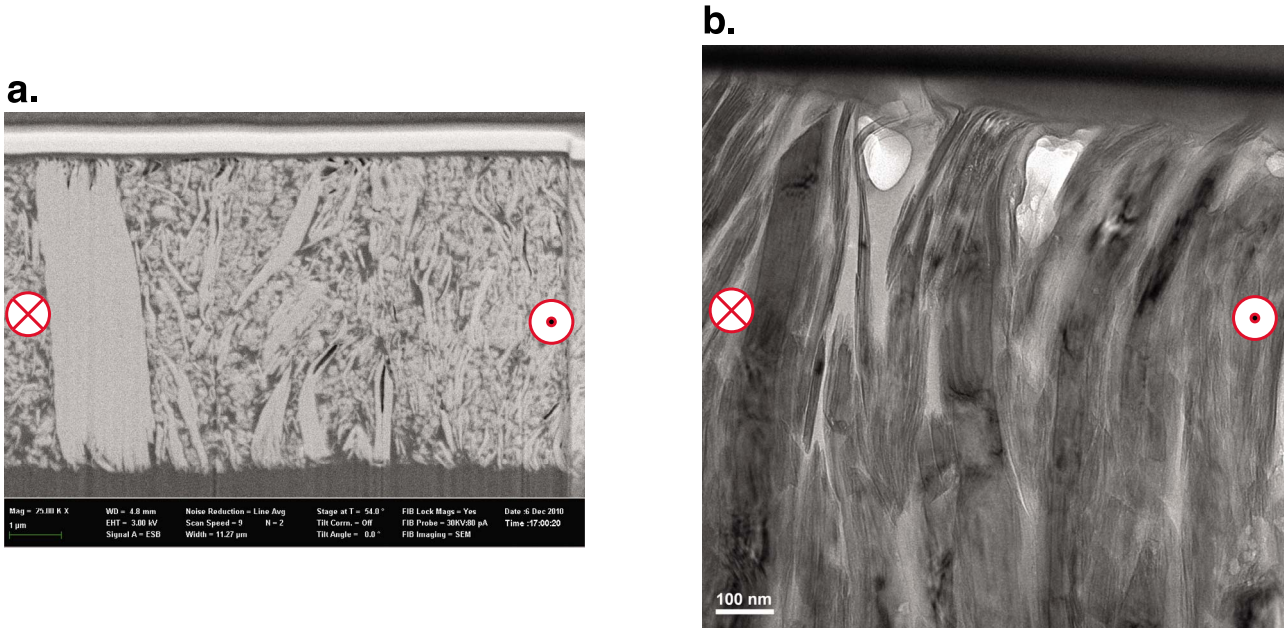

Figure 15. (a) SEM image (backscattered electron contrast at 3 kV) of a FIB-prepared cross section of the PSZ for dry conditions. Corresponding experiment (#1586) was stopped during the slip-weakening. A large number of nanometric aggregates can be observed within the PSZ. (b) TEM photomicrographs from FIB sections of the PSZ for wet conditions (#1472). No nanometric aggregate can be observed.

[*Hazzard and Mair*, 2003]. Microstructural observation indicates a strong interlayer delamination of talc as strain-induced defect. This suggests frictional sliding along the (001) cleavage planes [*Escartín et al.*, 2008; *Viti and Collettini*, 2009] as dominant deformation mechanism.

[50] In wet conditions, the absence of any C′-shear planes occurring in the central part of the fault gouge at any displacement, and the stable and high clast-to-matrix ratio (quantifying the amount of comminution) suggests that the amount of displacement accommodated by this part of the gouge is very small [*Mair and Marone*, 2000]. These observations indicate that the critical resolved shear stress needed to delaminate talc grains is rarely reached by grain sliding in the wet conditions. The absence of C′-shear planes and the lack of dilatancy could be explained by water capillary forces bridging the grain surfaces [*Velev et al.*, 1993; *Coelho and Harnby*, 1978; *Mizoguchi et al.*, 2006], resulting in the creation of strong adhesion forces to overcome gouge deformation.

[51] In dry conditions, some μm-thick subrounded grains show a cortex of irregular thickness made of very fine-grained aggregated material without any concentric arrangement as for Clast-Cortex Aggregates (see section 3.2.3). This suggests a structural immaturity of the aggregates. This immaturity is possibly related to the absence of rolling prevented from tightly packed grains.

[52] Deformation of the gouge in dry experiments appears to be more complex compared to wet experiments with the occurrence of stacked millimetric sigmoidal lenses bounded by open shear planes. These lenses show a surprisingly high C-S angle (>45°) of the internal fabric at 2 m of displacement, and this angle decreases with increasing displacement. This first characteristic indicates an antithetic rotation of the talc grains from an initial state similar to the wet case observed at 6 m of displacement (Figure 11d). Second, it indicates (more or less) intact lenses with an internal stress-insensitive fabric, suggesting the weakness of internal chain forces [*Daniels and Hayman*, 2008] and strain localization on the S-oriented shear planes delimiting individual lenses. These stacked lenses that frequently branch off from a single C-oriented shear plane clearly suggest a duplex system. Thus, similarly to natural fault gouges, the deformation spans the gouge system at the early stages of the fault displacement [*Hayman et al.*, 2004; *Hayman*, 2006]. The observed decrease of C-S angle of the internal fabric and increase in dilatancy, developing porosity along the open shear planes up to the residual shear stress at D_c, could be the result of accommodation of the geometric incompatibility of the stacked lenses, one lens sliding over the other. The decreasing clast-to-matrix ratio with the increasing displacement suggests that slip between individual grains is not as effective as in wet conditions, and that delamination of the talc grains occurs. As a result, the central part of the fault gouge accommodates a larger amount of displacement in dry conditions, compared to wet conditions. Initiation of lens formation might be controlled by some pre-existing gouge heterogeneities. But we do not have yet a complete understanding of this phenomenon.

[53] The μm-thick strongly foliated layers present at and parallel to the gouge-cylinder boundaries, whatever initial humidity conditions, indicate intense localized shearing in comparison to the central part of the gouge. This implies strain partitioning during fault displacement. This type of microstructure has already been reported in natural and experimental cases [*Yund et al.*, 1990; *Chester and Chester*, 1998; *Chambon et al.*, 2006; *Rockwell and Ben-Zion*, 2007; *Boutareaud et al.*, 2008; *Mizoguchi et al.*, 2009b; *Stünitz et al.*, 2010; *Kitajima et al.*, 2010] and was defined as the

Principal Slip Zone (PSZ) [*Sibson*, 2003], that controls earthquake instability [*Marone*, 1995; *Chester and Chester*, 1998; *Sibson*, 2003; *Rice*, 2006; *Boutareaud et al.*, 2008]. It is recognized to accommodate most of the displacement, and so should provide a path by which fault strength should weaken during shearing. The similarities in fabric of PSZ between wet and dry conditions and associated talc grain delamination suggests frictional sliding along the (001) planes [*Escartín et al.*, 2008; *Viti and Collettini*, 2009]. On the contrary, the differences in fabric (C-S structure for wet conditions and C- structure for dry conditions), suggest that a smaller amount of displacement is accommodated in wet conditions [e.g., *Trouw et al.*, 2010]. The PSZ thickness is in the range of calculated predictions for earthquake slipping zone width [*Rice*, 2006], and represents the source of the measured frictional heating [*Boutareaud et al.*, 2010; *Kitajima et al.*, 2010] reported here by *Tc* and *Tp*. The absence of any recognized phase transition product (i.e., enstatite) suggests that the temperature of PSZs was lower than 1300°C during experiments, or even lower than 860°C by comparison to previous dynamic data [*Escartín et al.*, 2008].

[54] Both wet and dry experiments show a slip-weakening behavior, but with a higher decreasing rate in wet conditions. Considering statements in the paragraph above, this indicates that water and related microstructure development should strongly affect strain accommodation in talc gouge at seismic slip-velocities.

[55] The relative slippage of the mm-long sigmoidal lenses in duplex structure is sufficient to explain the large dilatancy of the fault zone (up to 0.34 mm for the 1.3 mm-thick faults), and as direct consequence to explain the higher frictional strength for dry conditions during the slip-weakening [e.g., *Marone et al.*, 1990]. The maximum gouge layer dilation is proportional to the applied normal stress (Figure 9).

4.2. Identification of Slip-Weakening Mechanisms

[56] To date, several weakening mechanisms relevant for this type of friction experiment have been reported in the literature. This includes frictional melting [*Sibson*, 1980; *Hirose and Shimamoto*, 2005; *Di Toro et al.*, 2006; *Nielsen et al.*, 2008], silica gel production [*Goldsby and Tullis*, 2002; *Di Toro et al.*, 2004], thermal pressurization of the fluid [*Sibson*, 1973; *Rice*, 2006; *Boutareaud et al.*, 2008], fluid pressurization induced by thermal decomposition of the gouge material [*Sulem and Famin*, 2009; *Brantut et al.*, 2011], flash heating [*Rice*, 2006; *Beeler et al.*, 2008, *Goldsby and Tullis*, 2011], or powder lubrication [*Han et al.*, 2010, 2011; *Reches and Lockner*, 2010; *De Paola et al.*, 2011; *Tisato et al.*, 2012]. No evidence of amorphous material, silica gel, talc decomposition product (enstatite) has been observed in our post-run gouge products from petrographic microscope, SEM, TEM, cathodoluminescence, Raman spectroscopy or XRD observations. Therefore, neither frictional melting, flash heating, silica gel production, nor fluid pressurization induced by thermal decomposition of the gouge material appear to be the cause of the observed slip-weakening behavior, whatever humidity conditions. Thermal pressurization of the fluid, flash heating and powder lubrication remain as possible candidates as discussed below.

[57] The slip-weakening distance (D_c) of talc friction experiments decreases according to a power law for increasing normal stress (Figure 6). The slip-weakening behavior for talc is consistent with recent reported experiments conducted at coseismic slip-velocities from low (<25 MPa) to high (>25 MPa) normal stresses, regardless of fault rock type and related weakening mechanisms [*Mizoguchi et al.*, 2007a; *Brantut et al.*, 2008; *Han et al.*, 2010; *De Paola et al.*, 2011, *Niemeijer et al.*, 2011; *Oohashi et al.*, 2011]. The power law coefficients seem to be closely associated to the fault rock type [*Di Toro et al.*, 2011] and the activation of slip-weakening mechanisms [e.g., *Nielsen et al.*, 2008]. In our talc experiments, the power law dependence is established for the dry conditions at best ($R^2 = 0.87$), whereas no reasonable fit can be obtained for wet conditions suggesting the absence of significant thermally activated mechanisms in wet conditions.

[58] If any slip-weakening mechanism related to any efficient thermal-activation occurs during our experiments, D_c should scale with the fault power density (i.e., the energy exchanged on the PSZs per unit time and unit area equals to $1/(\tau.V)^2$). So D_c should scale with $1/(\tau.V)^2$ or $1/(\sigma^2.V)$ [e.g., *Del Gaudio et al.*, 2009]. Figure 8 supports such assumption for dry conditions only.

4.3. Proposed Slip-Weakening Mechanisms

[59] The gouge material we sheared in our experiments is not a rock composed of a solid framework with pores fill with water. The gouge material is a non-cohesive mixture of micrometric talc grains and water: it is a mud-like material. This continuum medium can be considered to be isotropic just before we start the experiment: the applied 1 MPa normal stress is supported by all the components of the medium (i.e., fluid and grains). So at first approximation, in the absence of leak, a 'fluid' pressure of 1 MPa can be considered when applying 1 MPa normal stress [see *Boutareaud et al.*, 2008]. According to the water phase diagram [*Wagner and Pruss*, 2002], the water liquid-to-vapor phase transition occurs at 180°C at a fluid pressure of 1 MPa. In Figure 4, our calculation shows that, in wet conditions, *Tp* reaches this transition temperature only after 3.84 s, i.e., after 5.03 m of displacement, which is posterior to *Dc* (see Table 1). In dry conditions, this temperature is reached by *Tp* after 0.31 s, i.e., after 0.40 m of displacement, which is anterior to D_c.

[60] Table 1 shows that D_c values of wet condition experiments are extremely short. For instance, on #1475 D_c is reached after only 3.72 m of displacement, which corresponds to 160°C for *Tp* and 37°C for *Tc* (Figure 4). This indicates a too low temperature along the fault plane to raise thermal pressurization by gouge water phase change from liquid to vapor during the slip-weakening [*Boutareaud et al.*, 2008: *Sulem and Famin*, 2009]. The absence of *i*) high-amplitude peak events in fault thickness (i.e., pulse-like events in fault axial displacement [e.g., *Mizoguchi et al.*, 2007b; *Boutareaud et al.*, 2008], *ii*) water vapor driven off from the simulated fault for displacements invariably smaller than D_c (Figure 2), concomitant with *iii*) the presence of immature Clast-Cortex Aggregates (see section 3.2.3) is consistent with such assumption.

[61] *Estimated* porosity of post-run central gouge is high (~10%) as well as the *dynamic* porosity (~15%), and a permeability value higher than 10^{-20} m^2 can be reasonably

expected considering that the initial gouge did not experience pressures higher than 30 MPa [*Behnsen and Faulkner*, 2011]. This suggests that the hydraulic diffusivity along the fault plane may be sufficient to raise thermal pressurization by thermal expansion of the gouge water during shearing [e.g., *Sibson*, 1973; *Wibberley and Shimamoto*, 2005; *Mizoguchi et al.*, 2009b]. Considering that the amount of displacement accommodated by the central part of the gouge and the PSZ is very small (see section 4.1), and the preservation of original large talc grains (see section 3.2.2), we propose thermal pressurization by thermal expansion of a water film in the early centimeters of displacement. This thin film of fluid should be trapped in-between two platy subparallel surfaces [e.g., *Morrow et al.*, 2000; *Moore and Lockner*, 2004; *Ferri et al.*, 2010]. Only the contact surface between the PSZ and the rotating cylinder satisfies the required condition for large displacement accommodation (see Figure 12c). However, regarding the hydrophobic character of talc, we suspect the existence of additional trapped water layers within the central gouge and the PSZ. Ensuing slip shows an increase of *Tp* at 5.03 m of displacement inducing a phase transition of water (180°C at 1 MPa fluid pressure) as indicated by an increase in measured humidity H (Figure 2e). We infer that the film of fluid is not anymore ubiquitous along the whole fault contact surface at these temperatures [e.g., *Moore et al.*, 1997], and we postulate solid lubrication [e.g., *Scholz*, 2006] to be the source of heating once the slip achieves the steady state at D_c. So we propose thermal pressurization by thermal expansion of a water film as a possible candidate for slip-weakening in wet conditions.

[62] The exponential decrease of the dynamic shear stress with increasing displacement (Figure 2) appears to be directly related to the progressive reorientation of grains parallel to the sense of shear and disappearance of the mm-long sigmoidal lenses toward the steady state stage at D_c (Figure 11). This indicates a progressive breakdown of the network chain forces through the whole gouge, involving localization of slip along the PSZ. To account for the progressive grain comminution shown by the decrease in clast-to-matrix ratio through central part of the gouge up to D_c (Figure 11, see section 3.2.2), the related temperature increase (Figure 4) and the long-lasting decay in fault strength (Figure 2), we propose a peculiar mechanism named solid lubrication [e.g., *Scholz*, 2006]. This mechanism consists in frictional sliding between the favorably C-oriented (001) planes of talc lamellae [*Escartín et al.*, 2008; *Viti and Collettini*, 2009] of the central part of the gouge and the PSZ. This mechanism is enhanced by thermal delamination resulting from exponential frictional heating rate (Figure 4), as suggested by opening of the cleavage of talc grains observed after long-duration cathodoluminescence examinations, probably caused by thermal expansion along the talc crystallographic *c* axis [*Pawley et al.*, 1995]. The observed nanometric aggregates represent an additional possibility to lubricate the simulated faults during the experiments by rolling and shearing (see section 3.2.2). The mode of formation of the nanometric aggregates is not totally understood. However, development of the nanometric aggregates (and consecutively the importance of the slip-weakening) is likely to be dependent on the talc sublamellae production by temperature rise as slip increases.

[63] The existence of two types of nanometric aggregates, within the central gouge and the PSZ suggests the existence of at most an additional weakening mechanism (see section 3.2.2). The apparent soft aspect of the nanometric aggregates within the central gouge suggests rolling and shearing (Figures 13c and 13d). On the contrary, the apparent rigid aspect of the nanometric aggregates within the PSZ (Figure 14c) suggests rolling [e.g., *Wornyoh et al.*, 2007]. These two types of nanometric aggregates may have the capacity to accommodate relative motion between talc lamellae and sublamellae during shearing at the micro-scale, and so to reduce wear production and consecutive friction at the macro-scale. We use the term powder lubrication to account for the nano-scale lubrication.

4.4. Relevance of the Experiments

[64] Peak shear stress values and the slip-weakening behavior that we obtained on talc powder are consistent with similar data previously reported by several authors at co-seismic slip-rates and low normal stresses for cohesive an non-cohesive rocks [*Hirose and Shimamoto*, 2005; *Di Toro et al.*, 2006; *Mizoguchi et al.*, 2006; *Hirose and Bystricky*, 2007; *Boutareaud et al.*, 2008; *Han et al.*, 2007, 2010; *Sone and Shimamoto*, 2009; *Mizoguchi et al.*, 2009b; *Kitajima et al.*, 2010; *Han et al.*, 2011; *De Paola et al.*, 2011], irrespective to the crustal rock type and related physico-chemical processes. Additionally, differences or similarities in mechanical behavior between clay-rich simulated faults appear to be related to the prevalence of one mechanism over the others. Reported prevailing weakening mechanisms occurring within the slip zone and consistent with our experiments are thermal pressurization and nano-powder lubrication [e.g., *Mizoguchi et al.*, 2007a; *Brantut et al.*, 2008; *Faulkner et al.*, 2011; *Reches and Lockner*, 2010; *Han et al.*, 2010, 2011; *Kohli et al.*, 2011; *Di Toro et al.*, 2011].

[65] The peak shear stress observed at the onset of shearing during our experiments represents the failure of the gouge strength just before shear localization [e.g., *Paterson and Wong*, 2004; *Mair and Hazzard*, 2007; *Mair and Abe*, 2008]. We attribute the high values of peak shear stress to the absence of a well-developed preferred orientation of talc grains which would allow easy slip along the (001) cleavage plane and the absence of nanometric aggregates at this stage (see section 3.2.2). Teflon friction probably participates to this peak friction value [*Sawai et al.*, 2012]. The lower peak shear stress value in wet conditions is attributed to the presence of a water film trapped along the fault contact surface in-between the PSZ and the rotating cylinder. A representative slide-hold-slide experiment is reported in Figure 10. The aim of this test is not to investigate the occurrence of any healing mechanism since it has been recently shown that phyllosilicates do not re-strengthen during hold periods [e.g., *Carpenter et al.*, 2011]. This test is conducted to test the effect of preexisting gouge microstructures on subsequent slip. This experiment shows a decrease of the peak shear stress when slip is resumed. The peak shear stress value of the third strain-cycle is similar to the peak shear stress value of the second strain-cycle. This experiment suggests first that the gouge fabric development plays a major role on the observed slip-weakening during the first strain-cycle. Second, it indicates that the lower friction

of subsequent slips is related to pre-existing microstructures inherited from the first strain-cycle. These results are consistent with the work of *Collettini et al.* [2009]. These authors reported friction experiments conducted on phyllosilicate-rich gouge samples. They showed that the friction coefficient of a simulated fault with a well-developed foliation is remarkably lower than its powdered equivalent. These results are also coherent with the work of *Mair et al.* [2002]. These authors showed that gouge grain shape characteristics have the capacity to control fault frictional behavior by reducing macroscopic friction in the case of spherical grains in granular material under shear. At least, these results are in agreement with experimental results done on phyllosilicate-bearing simulated faults [e.g., *Bos and Spiers*, 2000; *Numelin et al.*, 2007; *Mizoguchi et al.*, 2009b] reporting a positive correlation between fabric development, shear localization and strain weakening.

[66] Depending on the prevailing fluid flow properties and permeability structure of the fault zone [e.g., *Wibberley et al.*, 2008; *Mitchell and Faulkner*, 2008], mechanical and chemical healing processes occur during the interseismic period [*Sibson*, 1989; *Bos and Spiers*, 2000, 2002; *Nakatani and Scholz*, 2004; *Gratier and Gueydan*, 2007; *Keulen et al.*, 2008]. These processes may have the capacity to wipe out pre-existing fabric of clay-rich fault gouge [*Rutter et al.*, 1986]. So that the gouge starts with a randomized fabric each time a faulting event occurs and localizes along the same gouge zone [e.g., *Boutareaud et al.*, 2010]. Therefore, the degree of preferred orientation of phyllosilicates within the slip zone and the presence of nanometric spherical aggregates represent two important factors that may control the fault mechanical properties during earthquakes.

[67] The strong initial strengthening we observe in our experiments at the first strain-cycle suggests that the absence of nanometric aggregates or pre-existing well-oriented phyllosilicates within the slip zone may determine the occurrence of a frictional barrier for rupture growth into large earthquakes. This strengthening may prevent temperature rise of the gouge during acceleration stage of earthquake faulting, and consecutively the development of thermally activated slip-weakening mechanisms [*Rice*, 2006; *Brantut et al.*, 2010; *Di Toro et al.*, 2011]. This work suggests that the presence of nanometric aggregates or pre-existing well-oriented phyllosilicates within the slip zone should be seriously considered on future theoretical studies of faulting.

5. Summary and Conclusions

[68] We report mechanical data and related microstructures from high-velocity friction experiments conducted on a natural pure talc gouge as simple analogue of the phyllosilicates that compose the gouge of some mature crustal faults. However, talc exhibits a more complex mechanical behavior and microstructural development than expected.

[69] Post-run thin sections show a pervasive 30 μm-thick layer of small talc grains with a shape preferred orientation (SPO) parallel to the fault boundary, irrespective of initial humidity conditions and total displacements. This layer named Principal Slip Zone (PSZ) results from strain localization. It accommodates most of the fault displacement and produces the heat. In wet conditions, fault gouge fabric exhibits a S-C structure evolving to a C- geometry at higher displacements. Dry experiments appear to be more elaborated with the occurrence of stacked millimetric sigmoidal lenses bounded by μm-thick open shear planes. These lenses progressively disappear with increasing fault displacement, leading to a C- structure in the fault central gouge. Deformation that initially spans the fault system is then progressively fully localized along the PSZ.

[70] All our experiments show a slip-weakening behavior. We propose that the abrupt slip-weakening observed in wet conditions is related to thermal-pressurization by thermal expansion of a water film trapped between talc grains. On the contrary, in dry conditions, the long-lasting weakening is interpreted to be due to the progressive disappearance of geometrically unfavorably oriented large lenses, competing with solid lubrication of favorably C-reoriented talc lamellae combined with nanopowder lubrication within the PSZ and the central gouge. Few studies based on natural and simulated faults report solid lubrication and nanopowder lubrication as possible weakening mechanisms. This feature is probably related to the superimposition of additional mechanisms occurring within the phyllosilicate-rich fault slip zone during the weakening. This suggests that more attention should be paid on gouge microstructures at the nanometric scale for future studies in order to discriminate the weakening mechanisms.

[71] During a co-seismic slip, the first meters of slip-rate increase are critical to overpass the strength barrier to develop the appropriate slip-weakening mechanism(s). Our friction experiments suggest that inherited gouge fabric from past fault sliding has the capacity to play a major role on the slip-weakening for subsequent slip.

[72] **Acknowledgments.** We express our sincere thanks to Emily Brodsky and Amy Kornberg for helping us getting the talc samples from VWR Company. This work would not have been possible without the high-quality thin sections made by Christophe Nevado (Geosciences Montpellier) and by Frowin Pirovino (ETH, Zürich). A.M.B. and S.B. are grateful to Olivier Romeyer (Plateforme d'Analyze Structurale, Université de Savoie) for his technical assistance using SEM. S.B. thanks Karsten Kunze (EMEZ, ETH Zurich) for his support with FIB, providing outstanding sections for TEM observations. M.A. and S.B. want to thank Martiane Cabié and Michael Jublot for their technical assistance during TEM observation at the CP2M in Marseille. We thank also Christian Mensing (ETH Zurich) for TG/DTA measurements. The first author gratefully acknowledges Georg Dresen, Neil Mancktelow, Laurent Louis, Andre Niemeijer, and Chris Spiers for their fruitful discussions on the background of these studies. M.P. wishes to thank Rüdiger Kilian and Renée Heilbronner for stimulating discussion. S.B. thanks Stephen Miller for his helpful comments on earlier drafts of the manuscript. Careful and constructive reviews by Dan Faulkner and Cristiano Collettini helped to improve and strengthen the manuscript. This research was partially funded by an INSU grant (BG/LG/2010–15; Alea, Risques et Catastrophes Telluriques) and by ANR (Programme Catastrophes Telluriques et Tsunamis, ACTS Taiwan, ANR-06-CATT-001-01).

References

Barrett, S. D. (2002), Software for scanning microscopy, *Proc. R. Microsc. Soc.*, *37*, 167–174.

Beeler, N. M., T. E. Tullis, and D. L. Goldsby (2008), Constitutive relationships and physical basis of fault strength due to flash heating, *J. Geophys. Res.*, *113*, B01401, doi:10.1029/2007JB004988.

Behnsen, J., and D. R. Faulkner (2011), Water and argon permeability of phyllosilicate powders under medium to high pressure, *J. Geophys. Res.*, *116*, B12203, doi:10.1029/2011JB008600.

Bizzarri, A. (2009), What does control earthquake rupture and dynamics faulting? A review of different competing mechanisms, *Pure Appl. Geophys.*, *166*, 741–776, doi:10.1007/s00024-009-0494-1.

Bos, B., and T. Spiers (2000), Effect of phyllosilicates on fluid-assisted healing of gouge-bearing faults, *Earth Planet. Sci. Lett.*, *184*, 199–210, doi:10.1016/S0012-821X(00)00304-6.

Bos, B., and C. J. Spiers (2002), Fluid-assisted healing processes in gouge bearing faults: Insights from experiments on a rock analogue system, *Pure Appl. Geophys.*, *159*, 2537–2566, doi:10.1007/s00024-002-8747-2.

Bouchon, M. (1997), The state of stress on some faults of the San Andreas system as inferred from near-field strong motion data, *J. Geophys. Res.*, *102*, 11,731–11,744, doi:10.1029/97JB00623.

Boutareaud, S. (2007), Slip-weakening mechanisms at high slip-velocities: Insights from analogue and numerical modellings, Ph.D. thesis, Univ. de Franche-Comté, Besançon, France.

Boutareaud, S., D. G. Calugaru, R. Han, O. Fabbri, K. Mizoguchi, A. Tsutsumi, and T. Shimamoto (2008), Clay-clast aggregates: A new textural evidence for seismic fault sliding?, *Geophys. Res. Lett.*, *35*, L05302, doi:10.1029/2007GL032554.

Boutareaud, S., T. Hirose, M. L. Doan, M. Andréani, and D. G. Calugaru (2009), Frictional behavior of talc at seismic slip rates: Preliminary results from high-velocity experiments, *Geophys. Res. Abstr.*, *11*, EGU2009-1948.

Boutareaud, S., A. M. Boullier, M. Andreani, D. G. Calugaru, P. Beck, S. R. Song, and T. Shimamoto (2010), Clay-clast aggregates, a new textural evidence for seismic faulting, *J. Geophys. Res.*, *115*, B02408, doi:10.1029/2008JB006254.

Brantut, N., A. Schubnel, J. N. Rouzaud, F. Brunet, and T. Shimamoto (2008), High-velocity frictional properties of a clay-bearing fault gouge and implications for earthquake mechanics, *J. Geophys. Res.*, *113*, B10401, doi:10.1029/2007JB005551.

Brantut, N., A. Schubnel, J. Corvisier, and J. Sarout (2010), Thermochemical pressurization of faults during coseismic slip, *J. Geophys. Res.*, *115*, B05314, doi:10.1029/2009JB006533.

Brantut, N., R. Han, T. Shimamoto, N. Findling, and A. Schubnel (2011), Fast slip with inhibited temperature rise due to mineral dehydration: Evidence from experiments on Gypsum, *Geology*, *39*, 59–62, doi:10.1130/G311424.1.

Calugaru, D. G., J. M. Crolet, A. Chambaudet, C. I. Calugaru, and F. Jacob (2003), Inverse problems for flow and transport in the framework of seismic research, *Cah. Phys.*, *XIV*, 9–24.

Carpenter, B. M., C. Marone, and D. M. Saffer (2011), Weakness of the San Andreas Fault revealed by samples from the active fault zone, *Nat. Geosci.*, *4*, 251–254, doi:10.1038/ngeo1089.

Chambon, G., J. Schmittbuhl, and A. Corfdir (2006), Frictional response of a thick gouge sample: 1. Mechanical measurements and microstructures, *J. Geophys. Res.*, *111*, B09308, doi:10.1029/2003JB002731.

Chester, F. M., and J. S. Chester (1998), Ultracataclasite structure and friction processes of the Punchbowl fault, San Andreas system, California, *Tectonophysics*, *295*, 199–221, doi:10.1016/S0040-1951(98)00121-8.

Coelho, M. C., and N. Harnby (1978), Moisture bonding in powders, *Powder Technol.*, *20*, 201–205, doi:10.1016/0032-5910(78)80049-7.

Collettini, C., A. Niemeijer, C. Viti, and C. Marone (2009), Fault zone fabric and fault weakness, *Nature*, *462*, 907–910, doi:10.1038/nature08585.

Daniels, K. E., and N. W. Hayman (2008), Force chains in seismogenic faults visualized with photoelastic granular shear experiments, *J. Geophys. Res.*, *113*, B11411, doi:10.1029/2008JB005781.

Del Gaudio, P., G. Di Toro, R. Han, T. Hirose, S. Nielsen, T. Shimamoto, and A. Cavallo (2009), Frictional melting of peridotite and seismic slip, *J. Geophys. Res.*, *114*, B06306, doi:10.1029/2008JB005990.

De Paola, N., T. Hirose, T. Mitchell, G. Di Toro, C. Viti, and T. Shimamoto (2011), Fault lubrication and earthquake propagation in thermally unstable rocks, *Geology*, *39*, 35–38, doi:10.1130/G31398.1.

Di Toro, G., D. L. Goldsby, and T. E. Tullis (2004), Friction falls towards zero in quartz rock as slip velocity approaches seismic rates, *Nature*, *427*, 436–439, doi:10.1038/nature02249.

Di Toro, G., T. Hirose, S. Nielsen, G. Pennacchioni, and T. Shimamoto (2006), Natural and experimental evidence of melt lubrication of faults during earthquakes, *Science*, *311*, 647–649, doi:10.1126/science.1121012.

Di Toro, G., R. Han, T. Hirose, N. De Paola, S. Nielsen, K. Mizoguchi, F. Ferri, M. Cocco, and T. Shimamoto (2011), Fault lubrication during earthquakes, *Nature*, *471*, 494–498, doi:10.1038/nature09838.

Di Toro, G., S. Mittempergher, F. Ferri, T. M. Mitchell, and G. Pennacchioni (2012), The contribution of structural geology, experimental rock deformation and numerical modeling to an improved understanding of the seismic cycle. Preface to the Special Volume "Physico-chemical processes in seismic faults", *J. Struct. Geol.*, *38*, 3–10, doi:10.1016/j.jsg.2012.01.025.

Djéran-Maigre, I., D. Tessier, D. Grunberger, B. Velde, and G. Vasseur (1998), Evolution of microstructures and of macroscopic properties of some clays during experimental compaction, *Mar. Pet. Geol.*, *15*, 109–128, doi:10.1016/S0264-8172(97)00062-7.

Escartín, J., M. Andreani, G. Hirth, and B. Evans (2008), Relationship between the microstructural evolution and rheology of talc at elevated pressure and temperature, *Earth Planet. Sci. Lett.*, *268*, 463–475, doi:10.1016/j.epsl.2008.02.004.

Evans, B. W., and S. Guggenheim (1988), Talc, pyrophyllite and related minerals, *Rev. Mineral.*, *19*, 225–294.

Faulkner, D. R., T. M. Mitchell, J. Behnsen, T. Hirose, and T. Shimamoto (2011), Stuck in the mud? Earthquake nucleation and propagation through accretionary forearcs, *Geophys. Res. Lett.*, *38*, L18303, doi:10.1029/2011GL048552.

Ferri, F., G. Di Toro, T. Hirose, and T. Shimamoto (2010), Evidence of thermal pressurization in high-velocity friction experiments on smectite-rich gouges, *Terra Nova*, *22*, 347–353, doi:10.1111/j.1365-3121.2010.00955.x.

Goldsby, D. L., and T. E. Tullis (2002), Low frictional strength of quartz rocks at subseismic slip rates, *Geophys. Res. Lett.*, *29*(17), 1844, doi:10.1029/2002GL015240.

Goldsby, D. L., and T. E. Tullis (2011), Flash heating leads to low frictional strength of crustal rocks at earthquake slip rates, *Science*, *334*, 216–218, doi:10.1126/science.1207902.

Gratier, J. P., and F. Gueydan (2007), Deformation in the presence of fluids and mineral reactions: Effects of fracturing and fluid-rock interaction on seismic cycles, in *Tectonic Faults, Agent of Change on a Dynamic Earth*, edited by M. R. Handy et al., pp. 319–356, Mass. Inst. of Technol. Press, Cambridge.

Grunberger, D., I. Djéran-Maigre, B. Velde, and D. Tessier (1994), Measurement through direct observation of kaolinite particle reorientation during compaction, *C.R. Acad. Sci., Ser. II*, *318*, 627–633.

Han, R., T. Shimamoto, T. Hirose, J. H. Ree, and J. Ando (2007), Ultra low friction of carbonate faults caused by thermal decomposition, *Science*, *316*, 878–881, doi:10.1126/science.1139763.

Han, R., T. Hirose, and T. Shimamoto (2010), Strong velocity weakening and powder lubrication of simulated carbonate faults at seismic slip rates, *J. Geophys. Res.*, *115*, B03412, doi:10.1029/2008JB006136.

Han, R., T. Hirose, T. Shimamoto, Y. Lee, and J. I. Ando (2011), Granular nanoparticles lubricate faults during seismic slip, *Geology*, *39*, 599–602, doi:10.1130/G31842.1.

Hayman, N. W. (2006), Shallow crustal fault rocks from the black Mountain detachments, Death Valley, CA, *J. Struct. Geol.*, *28*, 1767–1784, doi:10.1016/j.jsg.2006.06.017.

Hayman, N. W., B. A. Housen, T. T. Cladouhos, and K. Livi (2004), Magnetic and clast fabrics as measurements of grain-scale processes within the Death Valley shallow crustal detachment faults, *J. Geophys. Res.*, *109*, B05409, doi:10.1029/2003JB002902.

Hazzard, J. F., and K. Mair (2003), The importance of the third dimension in granular shear, *Geophys. Res. Lett.*, *30*(13), 1708, doi:10.1029/2003GL017534.

Heaton, T. H. (1990), Evidence for and implications of self-healing pulses of slip in earthquake rupture, *Phys. Earth Planet. Inter.*, *64*, 1–20, doi:10.1016/0031-9201(90)90002-F.

Hirose, T., and M. Bystricky (2007), Extreme dynamic weakening of faults during dehydration by coseismic shear heating, *Geophys. Res. Lett.*, *34*, L14311, doi:10.1029/2007GL030049.

Hirose, T., and T. Shimamoto (2005), Slip-weakening distance of faults during frictional melting as inferred from experimental and natural pseudotachylytes, *Bull. Seismol. Soc. Am.*, *95*, 1666–1673, doi:10.1785/0120040131.

Ji, C., D. V. Helmberger, D. J. Wald, and K. F. Ma (2003), Slip history and dynamic implications of the 1999 Chi-Chi, Taiwan, earthquake, *J. Geophys. Res.*, *108*(B9), 2412, doi:10.1029/2002JB001764.

Kanamori, H., and E. E. Brodsky (2004), The physics of earthquakes, *Rep. Prog. Phys.*, *67*, 1429–1496, doi:10.1088/0034-4885/67/8/R03.

Keulen, N., H. Stünitz, and R. Heilbronner (2008), Healing microstructures of experimental and natural fault gouge, *J. Geophys. Res.*, *113*, B06205, doi:10.1029/2007JB005039.

Kitajima, H., J. S. Chester, F. M. Chester, and T. Shimamoto (2010), High-speed friction of disaggregated ultracataclasite in rotary shear: Characterization of frictional heating, mechanical behavior, and microstructure evolution, *J. Geophys. Res.*, *115*, B08408, doi:10.1029/2009JB007038.

Kohli, A. H., D. L. Goldsby, G. Hirth, and T. Tullis (2011), Flash weakening of serpentinite at near-seismic slip rates, *J. Geophys. Res.*, *116*, B03202, doi:10.1029/2010JB007833.

Lapusta, N. (2009), The roller coaster of fault friction, *Nat. Geosci.*, *2*, 676–677, doi:10.1038/ngeo645.

Lee, W. H., H. Kanamori, P. C. Jennings, and C. Kisslinger (2002), *The International Handbook of Earthquake and Engineering Seismology*, 81 pp., Academic, Amsterdam.

Lexa, O. (2003), Numerical approaches in structural and microstructural analyses, PhD thesis, Charles Univ., Prague.

Lim, S. C., M. F. Ashby, and J. H. Brunton (1989), The effect of sliding conditions on the dry friction of metals, *Acta Metall. Mater.*, *37*, 767–772, doi:10.1016/0001-6160(89)90003-5.

Mair, K., and S. Abe (2008), 3D numerical simulations of fault gouge evolution during shear: Grain size reduction and strain localization, *Earth Planet. Sci. Lett.*, *274*, 72–81, doi:10.1016/j.epsl.2008.07.010.

Mair, K., and J. F. Hazzard (2007), Nature of stress accommodation in sheared granular material: Insights from 3D numerical modeling, *Earth Planet. Sci. Lett.*, *259*, 469–485, doi:10.1016/j.epsl.2007.05.006.

Mair, K., and C. Marone (2000), Shear heating in granular layers, *Pure Appl. Geophys.*, *157*, 1847–1866, doi:10.1007/PL00001064.

Mair, K., K. M. Frye, and C. Marone (2002), Influence of grain characteristics on the friction of granular shear zones, *J. Geophys. Res.*, *107*(B10), 2219, doi:10.1029/2001JB000516.

Marone, C. (1995), Fault zone strength and failure criteria, *Geophys. Res. Lett.*, *22*(6), 723–726, doi:10.1029/95GL00268.

Marone, C., C. B. Raleigh, and C. H. Scholz (1990), Frictional behavior and constitutive modeling of simulated fault gouge, *J. Geophys. Res.*, *95*, 7007–7025, doi:10.1029/JB095iB05p07007.

Mitchell, T. M., and D. R. Faulkner (2008), Experimental measurements of permeability evolution during triaxial compression of initially intact crystalline rocks and implications for fluid flow in fault zones, *J. Geophys. Res.*, *113*, B11412, doi:10.1029/2008JB005588.

Mizoguchi, K., T. Hirose, T. Shimamoto, and E. Fukuyama (2006), Moisture-related weakening and strengthening of a fault activated at seismic slip rates, *Geophys. Res. Lett.*, *33*, L16319, doi:10.1029/2006GL026980.

Mizoguchi, K., T. Hirose, T. Shimamoto, and E. Fukuyama (2007a), Reconstruction of seismic faulting by high-velocity friction experiments: An example of the 1995 Kobe earthquake, *Geophys. Res. Lett.*, *34*, L01308, doi:10.1029/2006GL027931.

Mizoguchi, K., M. Takahashi, K. Masuda, and E. Fukuyama (2007b), Fault strength drop due to phase transitions in the pore fluid, *Geophys. Res. Lett.*, *34*, L09313, doi:10.1029/2007GL029345.

Mizoguchi, K., T. Hirose, T. Shimamoto, and E. Fukuyama (2009a), Fault heals rapidly after dynamic weakening, *Bull. Seismol. Soc. Am.*, *99*, 3470–3474, doi:10.1785/0120080325.

Mizoguchi, K., T. Hirose, T. Shimamoto, and E. Fukuyama (2009b), High-velocity frictional behavior and microstructure evolution of fault gouge obtained from Nojima fault, southwest Japan, *Tectonophysics*, *471*, 285–296, doi:10.1016/j.tecto.2009.02.033.

Moore, D. E., and D. A. Lockner (2004), Crystallographic controls on the frictional behavior of dry and water-saturated sheet structure minerals, *J. Geophys. Res.*, *109*, B03401, doi:10.1029/2003JB002582.

Moore, D. E., D. A. Lockner, M. Shengli, R. Summer, and J. D. Byerlee (1997), Strengths of serpentinite gouges at elevated temperatures, *J. Geophys. Res.*, *102*, 14,787–14,801, doi:10.1029/97JB00995.

Morrow, C. A., D. E. Moore, and D. A. Lockner (2000), The effect of mineral bond strength and adsorbed water on fault gouge frictional strength, *Geophys. Res. Lett.*, *27*(6), 815–818, doi:10.1029/1999GL008401.

Nakatani, M., and C. H. Scholz (2004), Frictional healing of quartz gouge under hydrothermal conditions: 1. Experimental evidence for solution transfer healing mechanism, *J. Geophys. Res.*, *109*, B07201, doi:10.1029/2001JB001522.

Nielsen, S., G. Di Toro, T. Hirose, and T. Shimamoto (2008), Frictional melt and seismic slip, *J. Geophys. Res.*, *113*, B01308, doi:10.1029/2007JB005122.

Niemeijer, A., C. Marone, and D. Elsworth (2010), Fabric induced weakness of tectonic faults, *Geophys. Res. Lett.*, *37*, L03304, doi:10.1029/2009GL041689.

Niemeijer, A., G. Di Toro, S. Nielsen, and F. Di Felice (2011), Frictional melting of gabbro under extreme experimental conditions of normal stress, acceleration, and sliding velocity, *J. Geophys. Res.*, *116*, B07404, doi:10.1029/2010JB008181.

Noda, H., and T. Shimamoto (2005), Thermal pressurization and slip weakening distance of a fault: An example of the Hanaore fault, southwest Japan, *Bull. Seismol. Soc. Am.*, *95*, 1224–1233, doi:10.1785/0120040089.

Numelin, T., C. Marone, and E. Kirby (2007), Frictional properties of natural fault gouge from a low-angle normal fault, Panamint Valley, California, *Tectonics*, *26*, TC2004, doi:10.1029/2005TC001916.

Oohashi, K., T. Hirose, and T. Shimamoto (2011), Shear-induced graphitization of carbonaceous materials during seismic fault motion: Experiments and possible implications for fault mechanics, *J. Struct. Geol.*, *33*, 1122–1134, doi:10.1016/j.jsg.2011.01.007.

Panozzo, R. (1983), Two-dimensional analysis of shape-fabric using projections of digitized lines in a plane, *Tectonophysics*, *95*, 279–294, doi:10.1016/0040-1951(83)90073-2.

Paterson, M. S., and T. F. Wong (2004), *Experimental Rock Deformation: The Brittle Field*, 358 pp., Springer, Berlin.

Pawley, A. R., S. A. T. Redfern, and B. J. Wood (1995), Thermal expansivities and compressibilites of hydrous phases in the system MgO-SiO_2-H_2O: Talc, phase A and 10 Å phase, *Contrib. Mineral. Petrol.*, *122*, 301–307, doi:10.1007/s004100050129.

Pec, M., H. Stünitz, and R. Heilbronner (2012), Semi-brittle deformation of granitoid gouges in shear experiments at elevated pressures and temperatures, *J. Struct. Geol.*, *38*, 200–221, doi:10.1016/j.jsg.2011.09.001.

Piga, L., F. Villieras, and J. Yvon (1992), Thermogravimetric analysis of a talc mixture, *Thermochim. Acta*, *211*, 155–162, doi:10.1016/0040-6031(92)87015-3.

Reches, Z., and D. Lockner (2010), Fault weakening and earthquake instability by powder lubrication, *Nature*, *467*, 452–455, doi:10.1038/nature09348.

Rice, J. R. (2006), Heating and weakening of faults during earthquake slip, *J. Geophys. Res.*, *111*, B05311, doi:10.1029/2005JB004006.

Rice, J. R., N. Lapusta, and K. Ranjith (2001), Rate and state dependent friction and the stability of sliding between elastically deformable solids, *J. Mech. Phys. Solids*, *49*, 1865–1898, doi:10.1016/S0022-5096(01)00042-4.

Rockwell, T. K., and Y. Ben-Zion (2007), High localization of primary slip zones in large earthquakes from paleoseismic trenches: Observations and implications for earthquake physics, *J. Geophys. Res.*, *112*, B10304, doi:10.1029/2006JB004764.

Rutter, E. H., R. H. Maddock, S. H. Hall, and S. H. White (1986), Comparative microstructures of natural and experimentally produced clay-bearing gouges, *Pure Appl. Geophys.*, *124*, 3–30, doi:10.1007/BF00875717.

Saad, Y. (2003), *Iterative Methods for Sparse Linear Systems*, 2nd ed., 528 pp., Soc. for Indust. and Appl. Math., Philadelphia, Pa., doi:10.1137/1.9780898718003.

Sawai, M., T. Shimamoto, and T. Togo (2012), Reduction in BET surface area of Nojima fault gouge with seismic slip and its implication for the fracture energy of earthquakes, *J. Struct. Geol.*, *38*, 117–138, doi:10.1016/j.jsg.2012.01.002.

Scholz, C. H. (2006), The strength of the San Andreas fault: A critical analysis, in *Earthquakes: Radiated Energy and the Physics of Faulting*, *Geophys. Monogr. Ser.*, vol. 170, edited by R. Abercrombie et al., pp. 301–311, AGU, Washington, D. C., doi:10.1029/170GM30.

Shimamoto, T., and A. Tsutsumi (1994), A new rotary-shear high-speed frictional testing machine: Its basic design and scope of research (in Japanese with English abstract), *J. Struct. Geol.*, *39*, 65–78.

Sibson, R. H. (1973), Interactions between temperature and pore fluid pressure during earthquake faulting: A mechanism for partial or total stress relief, *Nature*, *243*, 66–68, doi:10.1038/physci243066a0.

Sibson, R. H. (1980), Power dissipation and stress levels on faults in the upper crust, *J. Geophys. Res.*, *85*, 6239–6247, doi:10.1029/JB085iB11p06239.

Sibson, R. H. (1989), Earthquake faulting as a structural process, *J. Struct. Geol.*, *11*, 1–14, doi:10.1016/0191-8141(89)90032-1.

Sibson, R. H. (2003), Thickness of the seismic slip zone, *Bull. Seismol. Soc. Am.*, *93*, 1169–1178, doi:10.1785/0120020061.

Smith, S. A. F., A. Billi, G. Di Toro, and R. Spiess (2011), Principal slip zones in Limestone: Microstructural characterization and implications for the seismic cycle (Tre Monti fault, Central Apennines, Italy), *Pure Appl. Geophys.*, *168*, 2365–2393, doi:10.1007/s00024-011-0267-5.

Sone, H., and T. Shimamoto (2009), Frictional resistance of faults during accelerating and decelerating earthquake slip, *Nat. Geosci.*, *2*, 705–708, doi:10.1038/ngeo637.

Stünitz, H., N. Keulen, T. Hirose, and R. Heilbronner (2010), Grain size distribution and microstructures of experimentally sheared granitoid gouge at coseismic slip rates: Criteria to distinguish seismic and aseismic faults?, *J. Struct. Geol.*, *32*, 59–69, doi:10.1016/j.jsg.2009.08.002.

Sulem, J., and V. Famin (2009), Thermal decomposition of carbonates in fault zones: Slip-weakening and temperature-limiting effects, *J. Geophys. Res.*, *114*, B03309, doi:10.1029/2008JB006004.

Tisato, N., G. Di Toro, N. De Rossi, M. Quaresimin, and T. Candela (2012), Experimental investigation of flash weakening in limestone, *J. Struct. Geol.*, *38*, 183–199, doi:10.1016/j.jsg.2011.11.017.

Trouw, R. A. J., C. W. Passchier, and D. J. Wiersma (2010), Atlas of mylonites and related microstructures, 322 pp., Springer, New York.

Velev, O. D., N. D. Denkov, V. N. Paunov, P. A. Kralchevsky, and K. Nagayama (1993), Direct measurement of lateral capillary forces, *Langmuir*, *9*, 3702–3709, doi:10.1021/la00036a056.

Viti, C., and C. Collettini (2009), Growth and deformation mechanisms of talc along a natural fault: A micro/nanostructural investigation, *Contrib. Mineral. Petrol.*, *158*, 529–542, doi:10.1007/s00410-009-0395-4.

Vrolijk, P., and B. A. van der Pluijm (1999), Clay gouge, *J. Struct. Geol.*, *21*, 1039–1048, doi:10.1016/S0191-8141(99)00103-0.

Wagner, W., and A. Pruss (2002), The IAPWS formulation 1995 for the thermodynamic properties of ordinary water substance for general and

scientific use, *J. Phys. Chem. Ref. Data*, *31*, 387–535, doi:10.1063/1.1461829.

Ward, R. J. (1975), Kinetics of talc dehydroxylation, *Thermochim. Acta*, *13*, 7–14, doi:10.1016/0040-6031(75)80061-X.

Wesolowski, M. (1984), Thermal decomposition of talc: A review, *Thermochim. Acta*, *78*, 395–421, doi:10.1016/0040-6031(84)87165-8.

Wibberley, C. A. J., and T. Shimamoto (2005), Earthquake slip weakening and asperities explained by thermal pressurization, *Nature*, *436*, 689–692, doi:10.1038/nature03901.

Wibberley, C. A. J., G. Yielding, and G. Di Toro (2008), Recent advances in the understanding of fault zone internal structure: A review, in *The Internal Structure of Fault Zones: Implications for Mechanical and Fluid-Flow Properties*, edited by C. A. J. Wibberley et al., *Geol. Soc. Spec. Publ.*, *299*, 5–33.

Wintsch, R. P., R. Christoffersen, and A. K. Kronenberg (1995), Fluid-rock reaction weakening of fault zones, *J. Geophys. Res.*, *100*, 13,021–13,032, doi:10.1029/94JB02622.

Wornyoh, E. Y. A., V. K. Jasti, and C. F. Higgs (2007), A review of dry particulate lubrication: Powder and granular materials, paper presented at STLE/ASME 2006 International Joint Tribology Conference, Tribol. Div., San Antonio, Tex.

Yund, R. A., M. L. Blanpied, T. E. Tullis, and J. D. Weeks (1990), Amorphous material in high strain experimental fault gouges, *J. Geophys. Res.*, *95*, 15,589–15,602, doi:10.1029/JB095iB10p15589.